中國機械工程學刊第四十四卷第六期第 533~554 頁(民國一百一十二年)
Journal of the Chinese Society of Mechanical Engineers, Vol.44, No.6, pp533~554 (2023)

Non-Linear Dynamic Model and Analysis of Two-Speed Helical Gear Transmission Equipped with Two-Way Synchronizer

Linjun Tong*, AL-TAYARI ABDULHAMEED M.Y. **, Siyu Chen***and Zhou Sun**

Keywords: Pure Electric Vehicle, Two Speed Transmission, Two-way synchronizer, Non-linear dynamic model, Vibration response analysis.

ABSTRACT

In response to environmental pressure and market demand, multi-stage transmission is a feasible transmission mode for Pure Electric Vehicles (PEVs). Synchronizers can effectively reduce the vibration impact of PEV during frequent gear shifting, but the lack of a theoretical model limits the further study of its influence mechanism. Hence, a 20-degree-of-freedom (DOF) non-linear dynamic model of a two-speed helical gear (TSHG) transmission equipped with a two-way synchronizer is established considering the stiffness and friction torque of bidirectional synchronizer, time-varying meshing stiffness (TVMS), meshing damping, static transmission error (STE), gear backlash, torsional damping, and stiffness. The comparison with the experiment indicates the effectiveness of the established dynamic model. The results of the dynamics characteristics show that compared with the (low-speed) first gear transmission, the (high-speed) second gear transmission shows complex nonlinear dynamic characteristics. The increase in support stiffness, the decrease in TVMS ratio and STE amplitude contribute to the weakening and disappearance of the chaotic motion in the system. These results provide a helpful reference for non-linear behavior restraining and vibration and noise reduction of the two-speed transmission (TST) for PEVs.

Paper Received June, 2022. Revised July, 2023.Accepted August, 2023. Author for Correspondence: LinJun Tong.

* *Associate Professor, Department of Automotive Engineering, Foshan, Polytechnic, Foshan,Guangdong 528137, China.*

** *Graduate Student, Department of Mechanical and Electrical Engineering, Ccntral South University, Changsha, Hunan 410083, China.*

****Professor, Department of Mechanical and Electrical Engineering, Central South University, Changsha, Hunan 410083, China.*

INTRODUCTION

As environmental pollution, fossil fuel and green-gas shortages are some of the challenging issues for the eco-friendly new energy automotive world, PEVs (Hu et al., 2015), hybrid electric vehicles (HEVs) (Awadallah et al., 2017; Climent et al., 2021), and fuel cell electric vehicles (FCEVs) (İnci et al., 2021) have attracted world-wide's attention due to their remarkable advantages. Such as low noise, low or zero-emission energy saving, and high efficiency (Tseng and Yu, 2015; Wang et al., 2022; Huang et al., 2023). However, the energy density of electric batteries is much less than that of fossil fuels is still one of the challenges for EVs, which dramatically limits the new energy vehicle's drive mileage range (Mousavi et al., 2015). Recently, single-speed transmissions are equipped in most commercial PEVs due to their simple configuration, compact volume, and low manufacturing cost (Collins et al., 2018). Nevertheless, this type of transmission has obvious drawbacks due to the compromise between efficiency (drive mileage range) and dynamic performance (i.e., maximum speed, acceleration, and hill-climbing ability) (Han et al., 2019; Tian et al., 2020; Di et al., 2012). With the increasing demands, PEVs must provide a high level of safety, reliability, and ride comfort as well as satisfy without compromise regarding lightweight, recharge mileage, and low price (Karunamoorthy and Shobana, 2021; Alcazar-García et al., 2022). Therefore, the application of multiple-speed transmission in PEVs has received great attention. To meet these requirements, it is essential to further exploit the potential benefits of the electrified powertrain. Liang et al. (Liang et al., 2018; Li et al., 2016; Wang et al., 2017) have proved that multi-speed transmission systems are practical solutions to enhance the longitudinal behavior and overall efficiency of PEVs. Specifically, Gao's work (2022) demonstrated the advantages of two-speed transmissions in electric vehicles. Due to the balance between torque and speed, cars with two-speed transmissions perform excellently during overtaking and climbing. Two-speed transmission refers to the transmission having two gears: high and low. High-speed gears have relatively high rotational speeds and high energy consumption; Low-speed gears have relatively low rotational speeds and low energy consumption. Two-speed transmission has different transmission ratios, which can meet the needs of a larger output speed range. Since the PEVs integrated with a multi-speed transmission system can significantly cut energy consumption, improve drivability, save energy, make optimum use of high-efficiency motor operating ranges, and improve dynamic performance, a wide range of investigations have focused on exploring novel techniques and on improving the performance of existing systems (Ruan et al., 2016; Ahssan et al., 2018; Gao et al., 2015; Cao et al., 2019; S. Aldo et al., 2011; Qiong et al., 2013; Zhang et al., 2022).

The establishment of a dynamic model and vibration analysis of gear transmission systems have attracted a lot of attention. For instance, Hong et al. (2022) established a simulation model of a two-speed transmission with a rear friction clutch to study the driving dynamics and riding comfort during gear shifting. Ma et al. (2022) established a dynamic model of a two-speed transmission system equipped with planetary gears and toothed band brakes and investigated the impact of shifting strategies on the dynamic characteristics of the system. Li et al. (2023) have constructed a new type of mechanical-electro-hydraulic coupling system for electric vehicles to improve the stability of system operation. Long et al. (2022) conducted a whole vehicle dynamics simulation of PEVs to optimize the optimal dynamic shift point based on the relationship between acceleration and speed. Al Tayari et al. (2020) presented a non-linear dynamic model of SST for PEVs that consists of 16-DOF, including most of the non-linear factors in which the equation of motion was solved by the Runge–Kutta method. the effects of backlash, pinion rotating speed, torque fluctuation, and torsional stiffness on the dynamic behavior of the SST system were studied. Ma et al. (2018, 2019) developed a 14-DOF dynamic model including TVMS, damping, backlash, and transmission error to study the non-linear dynamic response analysis of the SST space driving mechanism under a large inertia load. Walha et al. (2009) presented a 12-DOF dynamic model to investigate the non-linear dynamic responses of an SST system by applying the technique of linearization to decompose the system from non-linear to linear. The effect of variable tooth friction and stiffness, localized tooth crack, geometrical errors, and pitch and profile errors on the 26-DOF dynamic model was studied by Jia et al. (2003). The influences of gear eccentricity on transverse and torsional dynamic responses and the dynamic transmission errors were investigated (He et al., 2019). Walha et al. (2011) proposed a dynamic model of 27-DOF considering spline clearance, double-stage stiffness, and dry friction path to investigate the non-linear dynamic response of the system coupled with an automotive clutch. Mo et al. (2019, 2018) presented a dynamic analysis and control of a three-speed PEV with a harpoon-shift synchronizer as an alternative to the traditional cone clutch synchronizer, where the transient responses of the driveline system during the gear-shifting process of the harpoon shaft was investigated. To guarantee driving comfort and vehicle drivability and enhance the overall efficiency of electric vehicles, power and shifting control of a novel transmission for PEV studies was performed by Liang et al. (2018), where the effectiveness of the proposed shifting strategy is verified by a detailed mathematical model of multi-speed transmission system equipped with two motors. To enhance gearshift quality and ride comfort of electric vehicles, a practical dynamic and kinematic analysis of a power shift five-speed AMT equipped with a wet clutch study was presented by Galvagno et al. (2011). To reduce rattle noise in an automotive transmission, a calculation and simulation of the rattle noise of a five-speed gearbox helical gear were held based on the design parameters (Bozca, 2010) and an empirical model (Bozca and Fietkau, 2010).

To the best of our knowledge, most of the research in previous literature mainly focuses on the non-linear dynamic modeling analysis and gear-shifting strategy of the TST system that is equipped with various applications. Yet, limited studies have curry out the effect of gear non-linear dynamic response of TST equipped with synchronizer used in PEVs. This paper presents a non-linear dynamic model with 20-DOF of a TST system equipped with a two-way synchronizer to investigate the pinion's rotating speed, TVMS ratio, supporting stiffness, and STE amplitude on the dynamic response. The comparison with the established electric drive two-speed transmission test bench indicates the effectiveness of the established model. Finally, some key conclusions are summarized to guide the design of vibration and noise reduction for the two-speed transmission system.

Two-Way Synchronizer Model

To achieve a smoother gear shift in multi-gear transmissions, a synchronizer is used to align the speed of the transmission target shaft and the output gear (Chen and Tian, 2016). To seize the main actuation characteristics of the double-side synchronizer, its mechanism is simplified to include only the speed synchronization stage of engagement. The post-synchronization is considered to be completely locked, ignoring other states of engagement (Walker and Nong,2012).

Therefore, the synchronizer model is reduced to only a cone clutch, where the cone clutch torque is calculated as follows

$$T_{Si} = \frac{u_D R_C F_{axial}}{\sin \alpha} \tag{1}$$

here, T_{Si} represents the friction torque of the synchronizer's cone clutch. u_D, F_{axial} and α represent the dynamic friction coefficient, the synchronizer load, and the cone angle. The parameters of the synchronizer components are mentioned in Table 1.

Table 1. The parameters of the two-speed synchronized gearbox and electric vehicle components.

Parameter	Value	Parameter	Value	Parameter	Value
I_m (kg·m^2)	0.04	C_m(Nm·s/rad)	0.0015	K_{11}(N·m /rad)	3.3134×10^7
I_s (kg·m^2)	0.0113	C_0 (Nm·s/rad)	10	K_{12} (N·m /rad)	3.3134×10^7
I_{p1} (kg·m^2)	7.619×10-5	C_{11} (Nm·s/rad)	2.0916	K_2 (N·m /rad)	30000
I_{p2} (kg·m^2)	0.009	C_{12} (Nm·s/rad)	2.0916	K_3 (N·m /rad)	13600
I_{p0} (kg·m^2)	1.372×10-4	C_{m1} (N·s/m)	0.8064	K_s (N·m /rad)	1920.8
I_{g1} (kg·m^2)	0.006	C_{m2} (N·s/m)	0.8064	K_0 (N·m /rad)	10000
I_{g2} (kg·m^2)	8.711×10-5	C_{m0} (N·s/m)	3.2918	K_{m1} (N/ m)	4.676×10^8
I_{g0} (kg·m^2)	0.036	C_t (Nm·s/rad)	0.01	K_{m2} (N/ m)	5.256×10^8
I_h (kg·m^2)	1.398	c_{ijv} (N·s/m)	500	K_{m0} (N/ m)	6.623×10^8
I_v (kg·m^2)	135.120	C_2 (Nm·s/rad)	10	k_{ijv} (N/ m)	3.5×10^7
T_m(Nm)	250	C_3 (Nm·s/rad)	100	μ_D	0.3
T_{load} (Nm)	254.702	R_c(m)	0.0475	α (°)	7

The synchronizer mechanism is usually controlled in an on-off manner, where the applied load is used to power the mechanism. The balance of force and torque during actuation can quickly achieve engagement without the need for closed-loop control (Alizadeh and Boulet, 2014). This eliminates the need to model complex electro-mechanical systems to engage synchronizer mechanisms and simplify the need for complicated synchronizer models. The constant positive and negative load is controlled to simulate the control of the engagement. The possible participation states are as follows

$$F_{axial} = \begin{cases} P & Engaging \\ 0 & Neutral \\ -P & Disengaging \end{cases} \tag{1}$$

here, P represents the magnitude of the automatic load applied.

This article only considers the synchronizer mechanism control in the simplest form, and the P value is consistent with the typical value of 350 N found in (Walker and Zhang, 2011). It is assumed that the synchronizer mechanism will be successfully engaged when energized, which is the typical situation according to reference (Lovas et al., 2006). Therefore, use the on/off control to energize the synchronizer or release the synchronizer and move it to the neutral position.

Modeling of meshing helical gear pair

The modeling of meshing helical gear pairs in the TST system is introduced here. A meshing helical gear pair of the TSHG system is shown in Figure 1. The STE $e_j(t)$ is spread out into Fourier series with the meshing frequency as the fundamental frequency (Raghothama and Narayanan, 1999), which can be expressed as

$$e_j(t) = e_{0j} + \sum_{S=1}^{S}[E_{chj}\cos(\omega_{hj}t + \varphi_{chj}) + E_{shj}\sin(\omega_{hj}t + \varphi_{shj}) \tag{2}$$

here, e_{0j} is the constant amplitude of STE, S is the Fourier series. E_{chj} and E_{shj} are the cosine and sinusoidal components of STE. ϕ_{chj} and ϕ_{shj} are the phase angles of the cosine and sinusoidal components. The gear pair's excitation meshing frequency ω_{hj} is determined as follows (Zhao and Ji, 2015)

$$\omega_{hj} = \frac{\Omega_{pj}\, Z_{pj}}{60} \tag{3}$$

Where, Z_{pj} and Ω_{pj} represent the teeth number and rotational speed of pinion.

The TVMS $k_{mj}(t)$ is considered as periodic-waveforms under mesh frequency and expanded into Fourier series according to Ishikawa's method (Kahraman and Singh, 1991), and expressed as follows

$$k_{mj}(t) = k_{0j} + \sum_{S=1}^{S}[A_{ckj}\cos(\omega_{hj}t + \varphi_{ckj}) + A_{skj}\sin(\omega_{hj}t + \varphi_{skj})] \tag{4}$$

here, k_{0j} is the mean value of mesh stiffness. A_{ckj} and A_{skj} are the cosine and sinusoidal components of stiffness fluctuation amplitude. ϕ_{ckj} and ϕ_{skj} are the phase angles of the cosine and sinusoidal components. Then, the mean value of the meshing damping c_{mj} can be written as

$$c_{mj} = 2\zeta_j\sqrt{k_{mj}\frac{r_{pj}^2 r_{gj}^2\, I_{pj} I_{gj}}{\left(r_{pj}^2 I_{pj} + r_{gj}^2 I_{gj}\right)}} \tag{5}$$

Generally, the damping coefficient ζ_j is calculated as Rayleigh damping (Bozca, 2018) in the range of (0.03-0.17). $j = (1,2,0)$ denote the first, second, and fixed-gear pairs transmission.

If x_{mj} denotes the gear's relative meshing-displacement under the impact of the gear's non-linear backlash s_j (Bozca and Fietkau, 2010), the backlash function can be expressed as the following

$$f(x_{mj}) = \begin{cases} x_{mj} - s_j & x_{mj} > s_j \\ 0 & -s_j \le x_{mj} \le s_j \\ x_{mj} + s_j & x_{mj} < s_j \end{cases} \tag{6}$$

The dynamic mesh force F_{mj} of gear-pair along the line-of-action (LOA) can be represented by a series of meshing damping and TVMS as the following

$$F_{mj} = k_{mj}(t) f(x_{mj}) + c_{mj}\dot{x}_{mj}, \quad \begin{cases} F_{pjx} = a_{xj}F_{mj}, F_{gjx} = -F_{pjx} \\ F_{pjy} = a_{yj}F_{mj}, F_{gjy} = -F_{pjy} \\ F_{pjz} = a_{zj}F_{mj}, F_{gjz} = -F_{pjz} \end{cases} \tag{8}$$

here, $a_{xi} = sin(-\alpha_{ni})\,cos(\beta_i)$, $a_{yi} = cos(-\alpha_{ni})\,cos(\beta_i)$, and $a_{zi} = sin(\beta_i)$ represent the angles first and the second gear pair $i = (1,2)$. $a_{x0} = sin(\alpha_{n0} - \pi)\,cos(-\beta_0)$, $a_{y0} = cos(\alpha_{n0} - \pi)\,cos(-\beta_0)$, and $a_{z0} = sin(-\beta_0)$ represent the angles of the (final) fixed-gear pair. $\beta_i$and α_{ni} denote the helix angle and pressure angle. $(F_{pjx}, F_{pjy}, F_{pjz})$ and $(F_{gjx}, F_{gjy}, F_{gjz})$ represent the dynamic mesh force of both pinion (driving wheel) and gear (driven wheel) at the coordinate directions x, y and z, respectively.

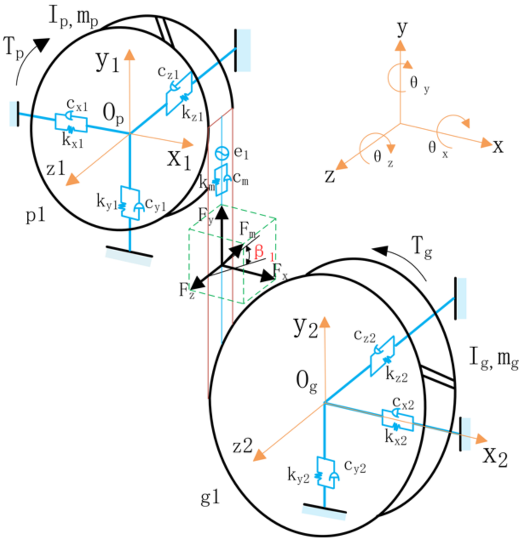

Fig. 1. Meshing model of a helical gear pair.

Dynamic model of the TSHG system

The research object of this paper is the integrated structure of a TST. This section adopts the equivalent concentrated mass method to simplify the vehicle transmission dynamics system, so the following assumptions are made:

(1) The rotational inertia of each component in the transmission system is regarded as a rigid inertial element, and the connection of the mass shaft is ignored.

(2) The flexural-torsional coupled vibration of rotating components is not considered.

(3) Ignore the influence of the quality of the drive shaft and the drive half shaft.

(4) It is assumed that there is no slip and slip between the wheel and the ground.

(5) Ignore the influence of oil stirring resistance during gear shifting.

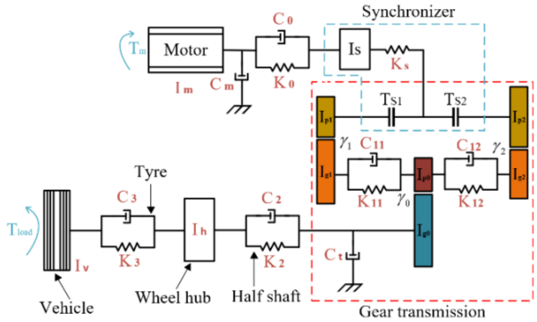

Fig. 2. Powertrain model of the two-speed electric vehicle equipped with a two-way synchronizer.

The TST powertrain system of the PEV equipped with a two-way synchronizer shown in Figure 2 is established as a multi-body model. The input shaft of the two-speed transmission is directly connected to the electric motor. In contrast, the output side of the gearbox assembly contains vehicle equivalent inertia, wheel hub, half shaft, the final drive, differential, etc. (Liang et al., 2018; Walker et al., 2017).

To represent the flexibility of the transmission input and output shaft, tires, and half-shaft, four spring dampers were employed in the model. In particular, there is no slip between the road and the belt (Bartram et al., 2010) due to the assumption that the tire belt is considered to be perfectly coupled to the road. The flexible connection between the rim and the tire's sidewall is denoted by a fixed stiffness and damping of a linear torsion spring damper (rather than a complex non-linear model). This model considers the rotational motion and does not consider the longitudinal and vertical movement of the tire and other PEV components.

To reduce the computational cost of the PEV dynamic model, it is assumed that the two branches (left and right half shafts and wheels) are symmetrical. As a result, when different synchronizers are engaged, the powertrain's rotational inertia and degrees of freedom will change. These inertial changes can be used to define the state of the powertrain. Taking the non-shifting state as an example, different states can be defined as follows:

Based on the assumption that there is no eccentricity in the transmission system and free body diagram, the differential equation of the input equation is derived as:

$$I_m\ddot{\theta}_m = T_m - K_0(\theta_m - \theta_s) - C_0(\dot{\theta}_m - \dot{\theta}_s) - C_m\dot{\theta}_m \quad (9)$$

where I_m represents the inertia of the motor, C_m denotes the viscous damping coefficient of the motor.θ_m represents the angular displacement, and its second derivative represents the rotation velocity and acceleration of the motor. C_0 and K_0 represent the damping and stiffness coefficients of the motor's shaft.

In the state of not shifting, the synchronizer is not fully engaged, and the dynamic equation of the synchronizer is as follows.

$$I_S\ddot{\theta}_S = K_0(\theta_m - \theta_s) + C_0(\dot{\theta}_m - \dot{\theta}_s) - K_s\theta_S - T_{S1} - T_{S2} \quad (10)$$

here, T_{si} is the torque produced from the synchronizer cone, K_s is the synchronizer stiffness, I_s is the inertia of the synchronizer, and θ_s is the torsional displacement of the synchronizer.

For half-axle tires and vehicle tires, since they are symmetrical and the equations on both sides are the same, only one side is described as

$$\begin{cases} I_h\ddot{\theta}_h = K_2(\theta_{g0} - \theta_h) + C_2(\dot{\theta}_{g0} - \dot{\theta}_h) - K_3(\theta_h - \theta_v) - C_3(\dot{\theta}_h - \dot{\theta}_v) \\ \qquad I_v\ddot{\theta}_v = K_3(\theta_h - \theta_v) + C_3(\dot{\theta}_h - \dot{\theta}_v) - T_{Load} \end{cases} \quad (11)$$

here, I_h represents the equivalent inertia of the wheel hub. I_v is the vehicle equivalent inertia, including tire inertia. θ_h and θ_v represent the torsional displacement of the synchronizer and vehicle tires, respectively. C_i and K_i represent the damping and stiffness coefficients of where $i = (2,3)$ denote the half-shaft and tire-wheel hub shaft, respectively.

The lumped dynamic equations of these transmission stages γ_1, γ_2 and γ_3 can be summarized as

$$\begin{aligned} I_{p1}\ddot{\theta}_{p1} + F_{m1}r_{p1}\cos(\beta_1) &= T_{S1} + T_{S2}I_{g1}\ddot{\theta}_{g1} + C_{11}(\dot{\theta}_{g1} - \dot{\theta}_{p0}) + K_{11}(\theta_{g1} - \theta_{p0}) + C_{12}(\dot{\theta}_{g2} - \dot{\theta}_{p0}) + K_{12}(\theta_{g2} - \theta_{p0}) \\ &\quad + F_{m1}r_{g1}\cos(\beta_1) = 0 \\ I_{p2}\ddot{\theta}_{p2} + F_{m2}r_{p2}\cos(\beta_2) &= T_{S1} + T_{S2}I_{g2}\ddot{\theta}_{g2} + C_{12}(\dot{\theta}_{g2} - \dot{\theta}_{p0}) + K_{12}(\theta_{g2} - \theta_{p0}) + C_{11}(\dot{\theta}_{g1} - \dot{\theta}_{p0}) + K_{11}(\theta_{g1} - \theta_{p0}) \\ &\quad + F_{m2}r_{g2}\cos(\beta_2) = 0 \\ I_{p0}\ddot{\theta}_{p0} - C_{11}(\dot{\theta}_{g1} - \dot{\theta}_{p0}) - K_{11}(\theta_{g1} - \theta_{p0}) &- C_{12}(\dot{\theta}_{g2} - \dot{\theta}_{p0}) - K_{12}(\theta_{g2} - \theta_{p0}) - F_{m0}r_{g0}\cos(-\beta_0) = 0 \\ I_{g0}\ddot{\theta}_{g0} - F_{m0}r_{g0}\cos(-\beta_0) &= -K_2(\theta_{g0} - \theta_h) - C_2(\dot{\theta}_{g0} - \dot{\theta}_h) - C_t\dot{\theta}_{g0} \end{aligned} \quad (12)$$

where I_{ij} is the equivalent inertia related to the transmission ratio, $i = (p, g)$ denote the driving gear (pinion) and driven gear (gear).$j = (0,1,2)$ represent the transmission ratio of the final drive, first, and second gear-pair, respectively. C_n and K_n represent the damping coefficient and stiffness coefficient of the low-speed $n = 11$ and high-speed $n = 12$ intermediate shafts, respectively.C_5 and K_5 are the damping coefficient and stiffness of the tire, and C_t represents the damping coefficient. γ_j represents the transmission ratio of j, and $j = (0,1,2)$ represents the gear ratios of the first gear, the second gear, and the final gear reduction, respectively.

Considering the new DOF mentioned above to the previous coordinate vectors of the two-stage gear reducer, the generalized coordinates vectors of the two-speed gearbox non-linear dynamic model increased to 20-DOF and defined as follows

$$\{q_m\} = \{\theta_m, \theta_s, \theta_h, \theta_v, \theta_{pn}, x_{pn}, y_{pn}, z_{pn}, \theta_{gn}, x_{gn}, y_{gn}, z_{gn}, \theta_{p0}, x_{p0}, y_{p0}, z_{p0}, \theta_{g0}, x_{g0}, y_{g0}, z_{g0}\}^T \quad (13)$$

where x_{ij}, y_{ij} and z_{ij} denote the translations of pinion and gear along axes x, y and z. θ_{ij}, θ_m, θ_s, θ_h and θ_v represent the torsional-displacement around the axis z of the (pinion p and gear g) at low-speed gear transmission, motor, synchronizer, half-axle, and vehicle tire, respectively. $n = (1,2)$ denotes the first and second gear shifting conditions. The parameters of the PEV and its transmission components are mentioned in Table 1 and Table 2.

Table 2. Continued-The parameters of the two-speed synchronized gearbox and electric vehicle components.

Parameter	Value	Parameter	Value
β_1, β_2, β_0 (°)	21.25, 21.25, 16.65	z_{p1}, z_{p2}, z_{p0}	25, 86, 29
ϕ_1, ϕ_2, ϕ_0 (°)	18.5, 18.5, 16.5	z_{g1}, z_{g2}, z_{g0}	77, 34, 91
r_{g1}, r_{g2}, r_{g0} (m)	0.0658, 0.0340, 0.0960	b_{g1}, b_{g2}, b_{g0} (m)	0.021, 0.022, 0.028
r_{p1}, r_{p2}, r_{p0} (m)	0.0214, 0.0861, 0.0306	b_{p1}, b_{p2}, b_{p0} (m)	0.0225, 0.0235, 0.030
M_1, M_2, M_3 (m)	0.00169, 0.00198, 0.00212	e_1, e_2, e_0 (μm)	20
s_1, s_2, s_0 (μm)	40	---	---

Considering the first gear shifting condition (low-speed transmission), synchronizer 1 (S_1) is engaged, and synchronizer 2 (S_2) is open, as shown in Figure 3. While synchronizer 2 (S_2) is engaged, synchronizer 1

(S_1) is open at the second gear shifting condition (high-speed transmission), as shown in Figure 4. After a complete synchronization process, the transmission is rigidly (closed) connected, and the lumped inertia of the synchronizer in Formula (10) and the first/second gear pair in Formula (12) are combined into Formula (14). Then, the torsional displacement of the synchronizer θ_m and pinion θ_{pi} are also combined into one torsional displacement.

$$(I_{p1} + I_S)\ddot{\theta}_{pj} = -F_{mi}r_{pi}\cos(\beta_i) + (K_0 + K_S)(\theta_m - \theta_{pi}) + (C_0 + C_m)(\dot{\theta}_m - \dot{\theta}_{pi}) + T_{Si} \tag{14}$$

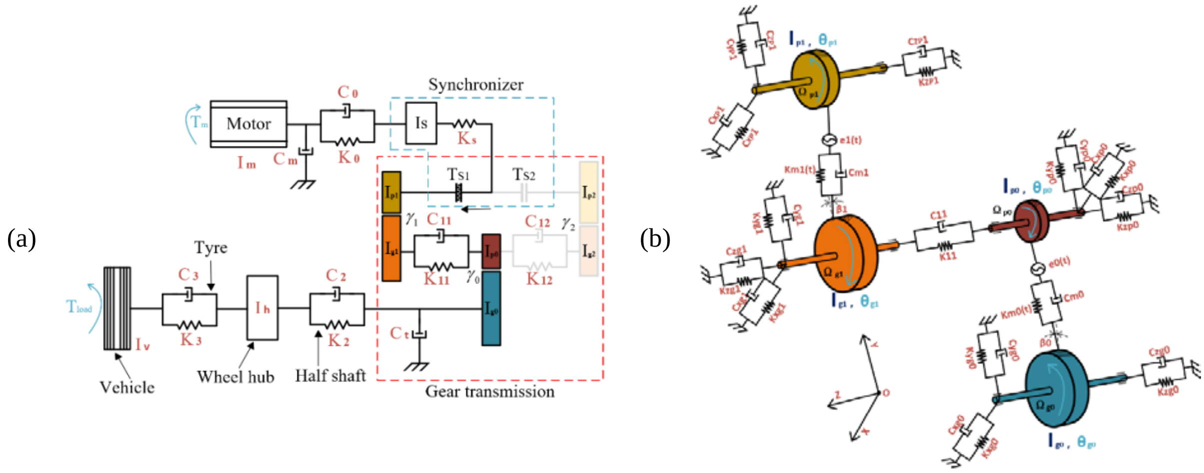

Fig. 3. The powertrain model of the electric vehicle system and gear pair transmission at the (low) first-speed transmission condition

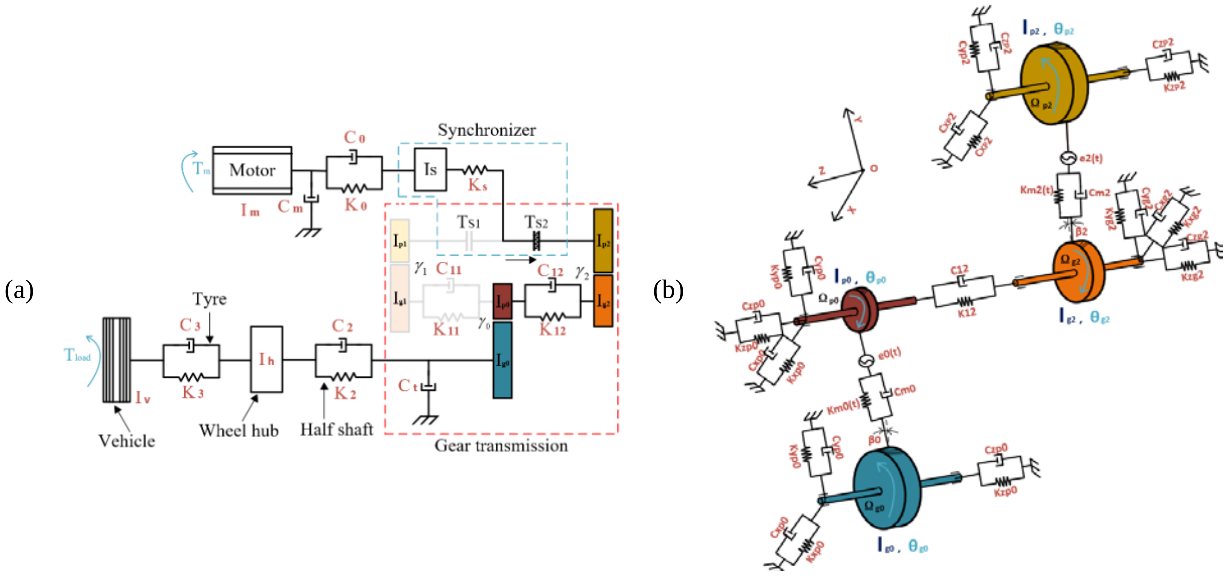

Fig. 4. The powertrain model of the electric vehicle system and gear pair transmission at the (high) second-speed transmission condition

After organizing the previous equation of the first gear shifting condition, the rotational and translational motion equations of the two-speed gearbox at the first/second transmission condition are listed as follows

$$
\begin{aligned}
I_m\ddot{\theta}_m &= T_m - (K_0 + K_s)(\theta_m - \theta_{pi}) - (C_0 + C_m)(\dot{\theta}_m - \dot{\theta}_{pi}) - T_{Si}(I_{pi} + I_S)\ddot{\theta}_{pi} \\
&= -F_{mi}r_{pi}\cos(\beta_i) + (K_0 + K_s)(\theta_m - \theta_{pi}) + (C_0 + C_m)(\dot{\theta}_m - \dot{\theta}_{pi}) + T_{Si}I_{gi}\ddot{\theta}_{gi} \\
&= -C_{1i}(\dot{\theta}_{gi} - \dot{\theta}_{p0}) - K_{1i}(\theta_{gi} - \theta_{p0}) - F_{mi}r_{gi}\cos(\beta_i)I_{p0}\ddot{\theta}_{p0} \\
&= C_{1i}(\dot{\theta}_{gi} - \dot{\theta}_{p0}) + K_{1i}(\theta_{gi} - \theta_{p0}) + F_{m0}r_{p0}\cos(-\beta_0)I_{g0}\ddot{\theta}_{g0} \\
&= F_{m0}r_{p0}\cos(-\beta_0) - K_2(\theta_{g0} - \theta_h) - (C_2 + C_t)(\dot{\theta}_{g0} - \dot{\theta}_h)I_h\ddot{\theta}_h \\
&= K_2(\theta_{g0} - \theta_h) + (C_2 + C_t)(\dot{\theta}_{g0} - \dot{\theta}_h) - K_3(\theta_h - \theta_v) - C_3(\dot{\theta}_h - \dot{\theta}_v)I_h\ddot{\theta}_h \\
&= K_3(\theta_h - \theta_v) + C_3(\dot{\theta}_h - \dot{\theta}_v) - T_{Load}
\end{aligned}
\tag{15}
$$

$$\begin{cases} m_{pi}\ddot{x}_{pi} + c_{xpi}\dot{x}_{pi} + k_{xpi}x_{pi} - a_{xi}F_{mi} = 0 \\ m_{pi}\ddot{y}_{pi} + c_{ypi}\dot{y}_{pi} + k_{ypi}y_{pi} + a_{yi}F_{mi} = 0 \\ m_{pi}\ddot{z}_{pi} + c_{zpi}\dot{z}_{pi} + k_{zpi}z_{pi} + a_{zi}F_{mi} = 0 \\ m_{gi}\ddot{x}_{gi} + c_{xgi}\dot{x}_{gi} + k_{xgi}x_{gi} + a_{xi}F_{mi} = 0 \\ m_{gi}\ddot{y}_{gi} + c_{ygi}\dot{y}_{gi} + k_{ygi}y_{gi} - a_{yi}F_{mi} = 0 \\ m_{gi}\ddot{z}_{gi} + c_{zgi}\dot{z}_{gi} + k_{zgi}z_{gi} - a_{zi}F_{mi} = 0 \\ m_{p0}\ddot{x}_{p0} + c_{xp0}\dot{x}_{po} + k_{xpo}x_{po} - a_{x0}F_{mo} = 0 \\ m_{p0}\ddot{y}_{po} + c_{ypo}\dot{y}_{po} + k_{yp0}y_{po} + a_{y0}F_{m0} = 0 \\ m_{p0}\ddot{z}_{p0} + c_{zpo}\dot{z}_{p0} + k_{zp0}z_{p0} - a_{z0}F_{m0} = 0 \\ m_{g0i}\ddot{x}_{g0} + c_{xg0}\dot{x}_{g0} + k_{xg0}x_{g0} + a_{x0}F_{m0} = 0 \\ m_{g0}\ddot{y}_{g0} + c_{yg0}\dot{y}_{g0} + k_{yg0}y_{g0} - a_{y0}F_{m0} = 0 \\ m_{g0}\ddot{z}_{gi0} + c_{zg0}\dot{z}_{g0} + k_{zg0}z_{g0} + a_{z0}F_{m0} = 0 \end{cases} \tag{7}$$

where m_{vw} indicates the mass $v = (p, g)$ in the first and second stages $w = (\mathrm{i}, 0)$, respectively.

The relative displacements of the first stage x_{m1}, the second stage x_{m2}, and (final) fixed stage x_{m0} along the LOA are defined as

$$x_{mi} = [(-x_{pi} + x_{gi})\,sin(-a_{ni}) + (y_{pi} - y_{gi})\,cos(-a_{ni}) + (r_{pi}\theta_{pi} + r_{gi}\theta_{gi})]\,cos(\beta_i) + (z_{pi} - z_{gi})\,sin(\beta_i) - e_i(t)$$

$$x_{m0} = [(-x_{p0} + x_{g0})\,sin(a_{n0} - \pi) + (y_{p0} - y_{g0})\,cos(a_{n0} - \pi) - (r_{p0}\theta_{p0} + r_{g0}\theta_{g0})]\,cos(-\beta_0) - (z_{p0} - z_{g0})\,sin(-\beta_0) - e_0(t) \tag{8}$$

For analytical convenience, a dimensionless form of the system equations above is derived by applying the following non-dimensional parameters as

$$\begin{cases} X_{ij} = \frac{x_{ij}}{s_j}, Y_{ij} = \frac{y_{ij}}{s_j}, Z_{ij} = \frac{z_{ij}}{s_j}, \\ X_b = \frac{x_b}{s_j}, E_j(\tau) = \frac{e_j(\tau)}{s_j}, \tau = \omega_n t \end{cases} \tag{9}$$

where $\omega_{nj} = \sqrt{k_{0j}/m_{ej}}$ indicates the natural frequency and $m_{ej} = I_{pj}I_{gj}/(I_{pj}r_{gi}^2 + I_{gj}r_{pi}^2)$ represents the equivalent mass of the gear pair. The small and big letter of each variable indicates the derivative to time t and dimensionless time τ , respectively.

Hence, the non-linear backlash function in the dimensionless form in Formula (7) becomes as

$$f(X_{mj}) = \begin{cases} X_{mj}(\tau) - 1 & X_{mj} > 1 \\ 0 & -1 \le X_{mj} \le 1 \\ X_{mj}(\tau) + 1 & X_{mj} < 1 \end{cases} \tag{10}$$

The dimensionless motion equation of the TST gear system in matrix form is expressed as

$$[\boldsymbol{M}]\{\ddot{\boldsymbol{Q}}_{\boldsymbol{m}}\} + [\boldsymbol{C}]\{\dot{\boldsymbol{Q}}_{\boldsymbol{m}}\} + [\boldsymbol{K}]\{\boldsymbol{Q}_{\boldsymbol{m}}\} = \{\boldsymbol{F}_{\boldsymbol{Q}}\} \tag{11}$$

where $[\boldsymbol{M}]$, $[\boldsymbol{C}]$, $[\boldsymbol{K}]$, $\{\boldsymbol{Q}_{\boldsymbol{m}}\}$ and $\{\boldsymbol{F}_{\boldsymbol{Q}}\}$ represent the mass matrix, damping matrix, stiffness matrix, coordinate vectors, and the external excitation force vectors of the dimensionless TST system. Their specific forms can be found in **APPENDIX A**.

Experimental Validation

This chapter takes the two-stage gear of the electric drive transmission as the experimental object, where the transmission vibration test bench is built according to the required design. We performed a dynamic vibration experiment on the test bench to verify the obtained theoretical analysis's validity. In the actual project, the system's vibration is generally reflected by the acceleration of the system or system components. Therefore, we use vibration acceleration to validate the theoretical model rather than transmission error.

This experiment adopts the vibration test and data collection analysis of "(the transmission box equipped with an acceleration sensor) (data collection system) (testing computer) (data processing and analysis)". The experimental setup and design scheme of the test bench are illustrated in Figure 5. Where the main structure of the test bench includes 1 input motor, 2 big belt pulley, 3 small belt pulley, 4 torque & speed sensor, 5 two-stage gearbox and 6 load motor. In this vibration experiment, the data collection part uses the SCM data acquisition system and related software designed and developed by LMS to measure and analyze the system's vibration data. The specific parameters of the test bench are shown in Table 3.

According to the chapter *Dynamic model of the TSHG system*, the dynamic modeling equation of the gear transmission system of the electric drive transmission is solved, and the vibration characteristics of the system under various simulation conditions are theoretically analyzed. Solving the dynamic equations in MATLAB can provide us with the system's vibration displacement and vibration velocity under various working conditions. Analyze the speed from 500-3000 rpm, taking an analysis speed every 250 rpm. The x-axis and y-axis represent the radial direction, and the z-axis represents the axial direction. The results of predicted and measured vibration accelerations concerning the rotational speed of the pinion are shown in Figure 6.

Table 3. Continued-The parameters of the two-speed synchronized gearbox and electric vehicle components.

Parameter	Value
Rated torque	95 Nm
Maximum load level	Level 13
Motor rated power	30 KW
Temperature control accuracy	±2 ℃
Temperature adjustment range	0-100 ℃
Motor speed	10-3000 r/min
Test gearbox capacity	1.8 L
Test machine size	1500×900×800 mm

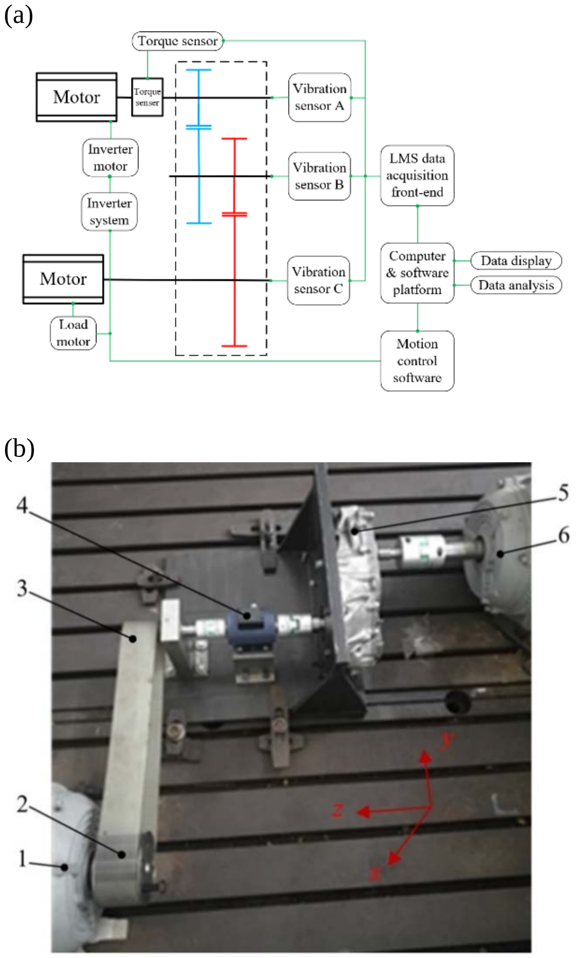

Fig. 5. Vibration test plan scheme

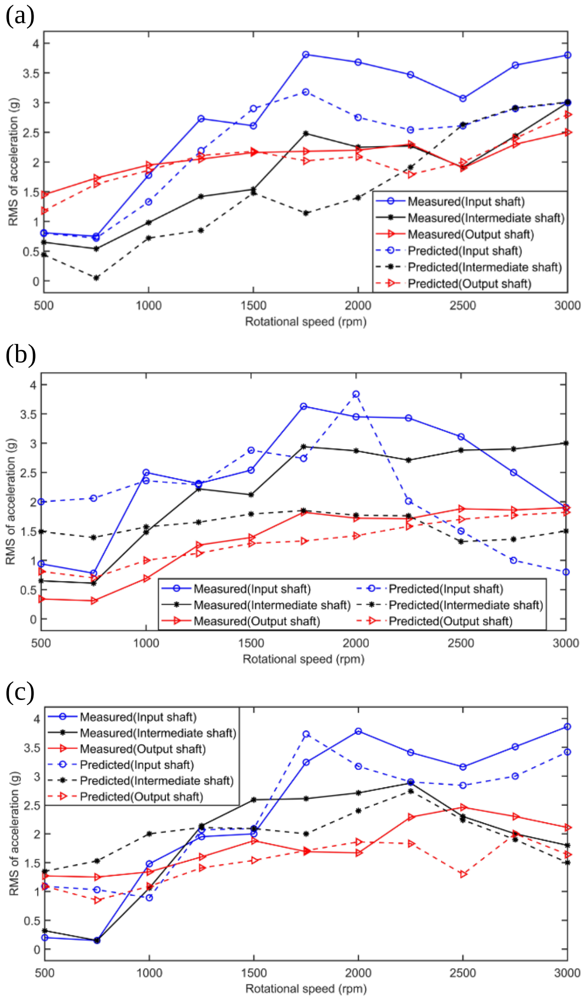

Fig. 6. Comparison of predicted and measured vibration acceleration concerning the rotational speed of pinion: (a) in x-axis direction, (b) in y-axis direction, (c) in z-axis direction.

Compared with the experimental results, when the rotational speed is greater than 1750 rpm, the RMS amplitude of the vibration acceleration of the three shafts obtained by theoretical analysis gradually decreases. It can be seen from Figure 6 (a) that the measured and predicted results of the vibration characteristics in the x-axis direction at low speed correspond well. Consequently, the difference between the predicted and measured vibration acceleration is relatively large as the rotating speed increases along to 3000 rpm, which may be related to the design of the actual gearbox transmission and testing method. However, compared with the input and intermediate shafts' vibration, the measured vibration acceleration of the output shaft corresponds well with the predicted vibration acceleration. In conclusion, it can be seen from the experimental results that the vibration of the system is the most severe when the speed is 1750 rpm. With the increase of rotating speed, the vibration acceleration of the three transmission shafts gradually increases, but the vibration acceleration decreases at 750, 1500, and 2500 rpm.

In the y-axis direction, the vibration of each shaft is shown in Figure 6 (b). When the rotating speed is low, the vibration acceleration value obtained from the theoretical analysis of the input shaft is quite different from the experimental measurement result. When the rotation speed is lower than 1250 rpm the predicted vibration acceleration of the shafts is larger than the measured vibration acceleration. At the rotating speed of 1000, 1250, and 1500 rpm, the measured acceleration vibration is in good agreement with the predicted vibration acceleration. After the rotating speed of 2000 rpm, the variation gap between the theoretical result and experimental result increases enlarges again, while the measured vibration acceleration is larger than the predicted vibration acceleration. The measured vibration acceleration of the output shaft corresponds well with the predicted vibration acceleration within the entire experimental speed range. The predicted and measured vibration accelerations in x-axis direction appear to be in good arguments when compared with the vibration acceleration in the y-axis direction.

The comparison figure of the predicted and measured vibration acceleration in the z-axis direction is shown in Figure 6 (c). It can be noticed that the theoretical analysis results and experimental measurement results of the three shafts of the system are consistent in trend, but there is a certain deviation in the result value. The theoretical calculation results of the output shaft and the experimental results are consistent at low speeds up to 1500 rpm, while the measured vibration acceleration of the input and intermediate shafts is lower than the predicted one. The theoretical and actual results of the output shaft show different trends at 2000 rpm and 2500 rpm. Even at 2500 rpm, the experimental result is about 3 times the theoretical calculation value. It may be related to the pasting direction of the acceleration sensor and the experimental environment.

In general, the vibration test results at each test point are consistent with the theoretical analysis and calculation results, and the vibration acceleration of each drive shaft has inevitable fluctuations at different speeds. However, as the speed gets higher, the transmission shaft's vibration and gearbox get more severe, proving that the dynamic analysis method and process obtained in the previous Chapter are correct and feasible.

RESULTS AND DISCUSSION

The effect of the rotating speed on the tow-speed gearbox transmission

The effect of the rotating speed on the tow-speed gearbox at the (low) first-speed transmission condition

The dimensionless motion equations are solved by applying the fourth-order Runge-Kutta numerical integration method in MATLAB (ODE-45 solver). The bifurcation diagrams are useful tools for observing the dynamic responses of the system (Wang et al., 2019). Figure 7 (a) and (b) show both forward and backward bifurcation characteristics in the dimensionless displacement of the system X_{m1} with the pinion rotating speed variation.

(a)

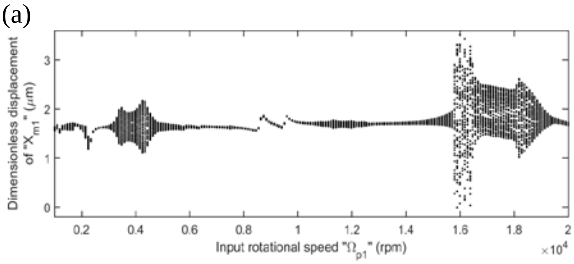

(b)

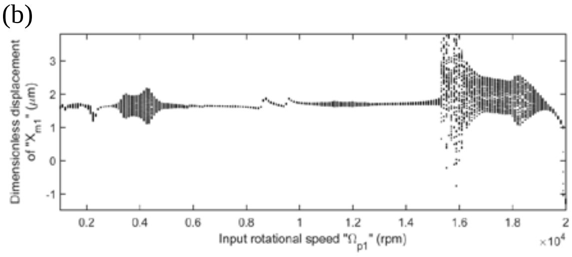

(c)

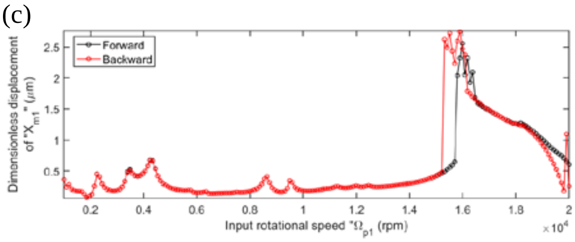

(d)

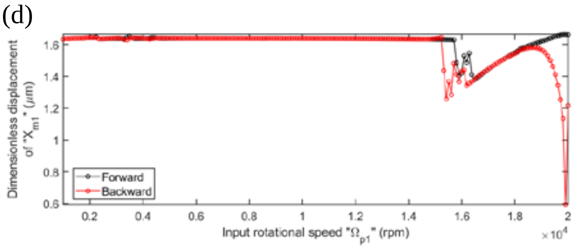

Fig. 7. The vibration diagrams of the system X_{m1} of the first-speed transmission using Ω_{p1} as a controller parameter: (a) forward bifurcation map, (b) backward bifurcation map, (c) PPV, (d) RMS.

To comprehend the dynamic behaviors more clearly, different diagrams such as amplitude-frequency spectrums, time response diagrams, and phase plane maps with poincaré points are presented. At the first gear shifting condition, when the pinion's rotating speed is low, it can be indicated that the response of X_{m1} is in a quasi-periodic motion and persists until it reaches 15700 rpm, where the phase portrait and poincaré map show shifted and thick response results, as displayed in Figure 8 (a). As the pinion's rotating speed increases to the range {3101-4915} rpm, the corresponding displacement of X_{m1} enrages, as displayed by the enlarged range of both poinceré points and phase plane, the fluctuation of time-domain history and the existence of the sidebands after the dominant peak 1 f_m in FFT (Fast Fourier Transform) spectra, as displayed in Figure 8 (b). When the rotating speed is within the range {15800-16470} rpm, the system enters a chaotic region through a quasi-periodic motion route. The amplitude-frequency spectrum is infinite continuous components (W. Chen et al., 2019), the phase plane diagram and time domain response diagram also show irregular motions that result in a chaotic response, and the poincaré point does not repeat itself in any pattern, as demonstrated in Figure 8 (c). When the rotating speed has increased to 16850 rpm, the system turns back to quasi-periodic motion and remains in the state with the decreasing of the displacement range until 20000 rpm. As shown in Figure 8 (d), the poincaré map's return points form a closed orbit and the phase plane diagram has a thick curve. These characteristics prove that the system is a quasi-periodic motion (Wang et al., 2019). Considering the backward bifurcation shown in Figure 7 (b), it is evident that the system response has the same trend compared with the forward bifurcation. The difference in the backward one is that the chaotic motion is enlarged and shifted forward to the speed range from 15320 rpm to 16090 rpm. A high amplitude of displacement exists at a very high speed at 19700 to 20000 rpm. While the poinceré points perform a thick linear line with shifted cycles that appear in one side of the phase plane, that is due to the fluctuation of the upper displacement amplitude of time-domain history, and a single synchronous frequency appears in the FFT plot, as shown in Figure 8 (e). These phenomena indicate that the system has the most impact at high rotating speed.

The peak-to-peak value (PPV) and root mean square (RMS) curves of the system X_{m1} at the first condition concerning rotating speed are illustrated in Figure 7 (c) and (d). The dynamic response has many prominent sub-harmonic peaks (B. Fan et al., 2018) occurring at {2241, 3482, 4246, 8638, 9497} rpm. In response to the non-linear system, the phenomenon of ‘frequency hopping’ usually exists in the bifurcation diagram. In the case of the forward sweep, a ‘frequency hopping’ phenomenon is obtained around the response frequency of speed at 15700 rpm, whereas another ‘frequency hopping’ phenomenon occurred around 14650 rpm in the case of the backward sweep. Moreover, a hysteresis loop (Chen et al., 2019) can be observed in PPV and RMS curves, and two apparent bistable response regions are noted around {15230-15700} rpm and {18100-20000} rpm.

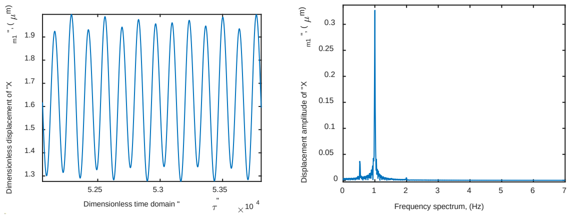

Time-domain response FFT spectrum

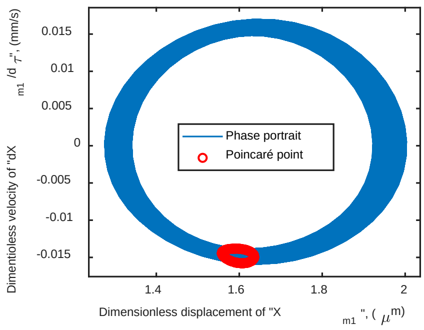

Phase plane and poincaré point

(a)The dynamic response of the system X_{m1} at 1000 rpm

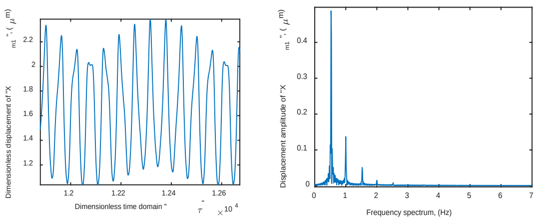

Time-domain response FFT spectrum

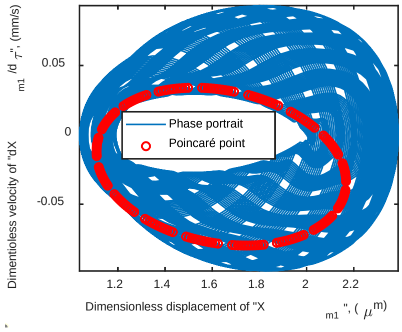

Phase plane and poincaré point

(b)The dynamic response of the system Xm1 at 4246 rpm

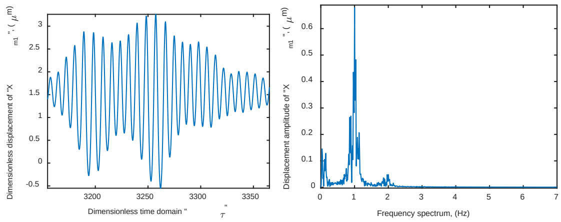

Time-domain response FFT spectrum

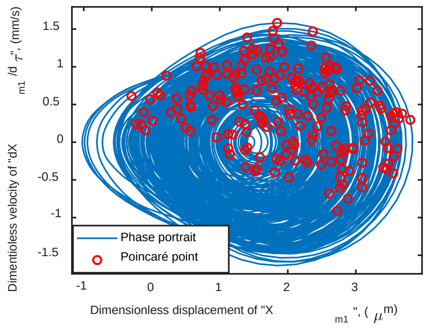

Phase plane and poincaré point

(c)The dynamic response of the system Xm1 at 16000 rpm

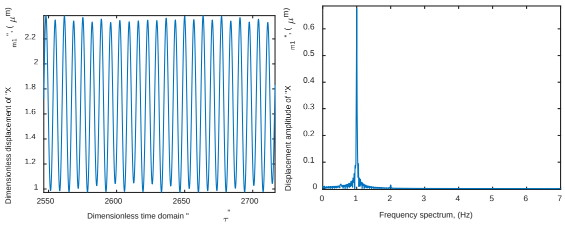

Time-domain response FFT spectrum

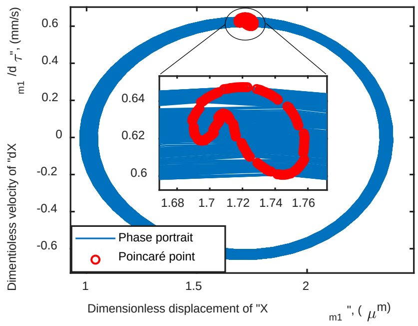

Phase plane and poincaré point

(d)The dynamic response of the forward sweep system Xm1 at 19800 rpm

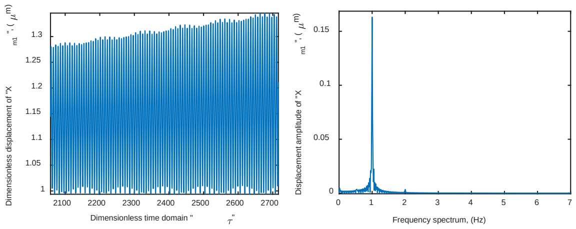

Time-domain response FFT spectrum

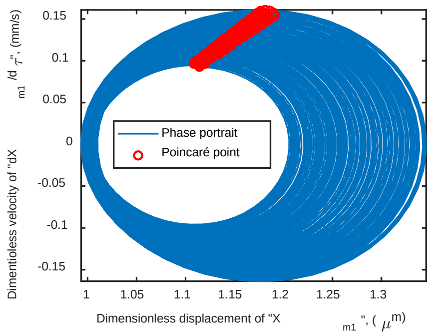

Phase plane and poincaré point

(e)The dynamic response of the backward sweep system X_{m1} at 19800 rpm

Fig. 8. The dynamic response of the system X_{m1}

With the variating of rotating speed, the system X_{m0} behaves as quasi-periodic motion that remains in this state from 1000 rpm to 15400 rpm, as shown in Figure 7 (a) and (b). In this case, the phase plane diagram has a thick track circle where the return points in the poincaré section corresponding to 1000 rpm show a loop with a closed phase. The meshing frequency f_m was still the dominant response where the combination components and frequency multiplication of variable frequencies were observed. The above characteristics indicate that the system is in a quasi-periodic motion (Pan et al., 2019), as illustrated in Figure 10 (a). After a long quasi-periodic motion state, the system turns into chaotic motion rapidly at a high-speed range from 15510 rpm to 17450 rpm. The time-domain response diagram and phase plane diagram show chaotic attractors with random distribution characteristics. The return points in poincaré maps form an unordered point set. The meshing frequency f_m was no longer the dominant response where the FFT spectra show a continuous broadband response. These vibration features prove that the system is in a state of chaos, as shown in Figure 10 (b). After undergoing the chaos state, the system turns back into quasi-periodic motion until the speed reaches 20000 rpm. Here, the phase plane portrait is trajectory torus with phase-locked loops shown in the poincaré section, non-integer multiple of mesh frequency appears in FFT spectra, and the time domain response diagram shows fluctuated periodic motion. These characteristics prove that the system is in quasi-periodic motion, as shown in Figure 10 (c).

The PPV and RMS curves of the system X_{m0} at the first condition with respect to rotating speed are illustrated in Figure 7 (c) and (d). The dynamic system response has many noticeable (resonant motion) sub-harmonic peaks occurring about {2241, 3387, 4342, 8638, 9497} rpm. During the forward sweep, a jump-down phenomenon was observed around the response frequency of speed 14560 rpm, while a jump-up one occurs around the response frequency of speed 15510 rpm. Due to the disparity of backward bifurcation's characteristics, hysteresis loops occur in PPV and RMS maps while the bistable response regions are determent within {14560-15510} rpm and {19050-20000} rpm.

In summary, the dynamic responses of the systems X_{m1} and X_{m0} of the first condition are identical. Under the variation of the rotational speed, both systems behave as a quasi-periodic motion. Excluding when the speed at the range of {14650-16090} rpm for system X_{m1} and {14560-17420} rpm for system X_{m1}, both systems become unstable and change into chaotic motions. Comparing the forward and backward bifurcation, the range of chaotic response of both systems X_{m1} and X_{m0} during the forward sweep enlarges and shifts forward during the backward sweep, as proven by the bistable response regions and amplitude of PPV and RMS maps.

(a)

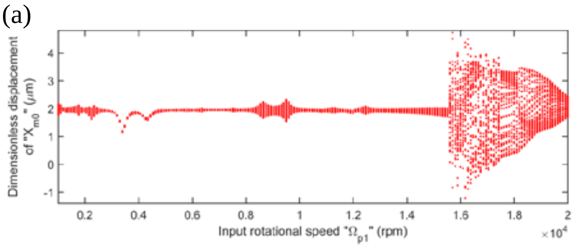

(b)

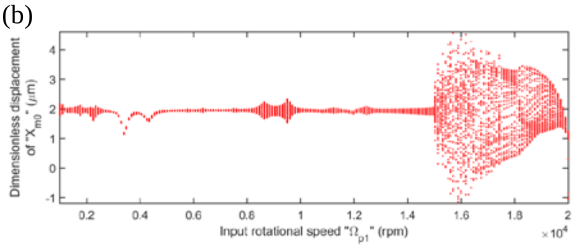

(c)

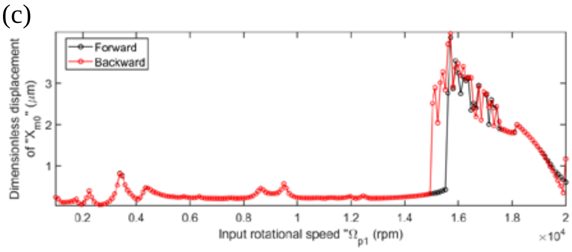

(d)

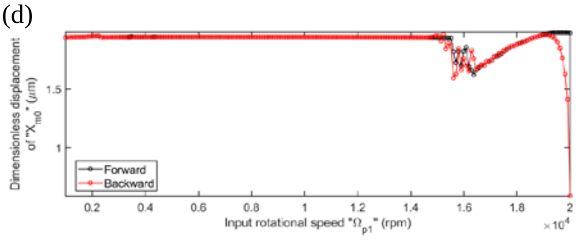

Fig. 9. The vibration diagrams of the system X_{m0} of the first-speed transmission using Ωp1 as a controller parameter: (a) forward bifurcation map, (b) backward bifurcation map, (c) PPV, (d) RMS.

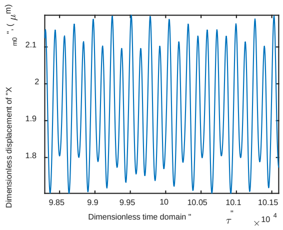

Time-domain response

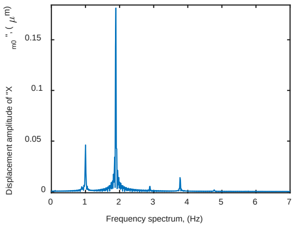

FFT spectrum

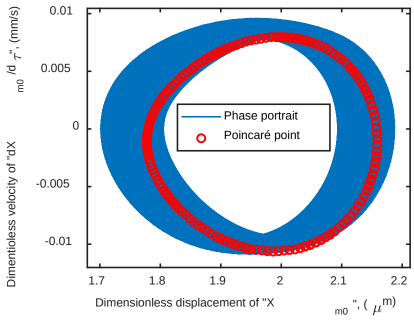

Phase plane and poincaré point

(a)The dynamic response of the system X_{m0} at 1000 rpm

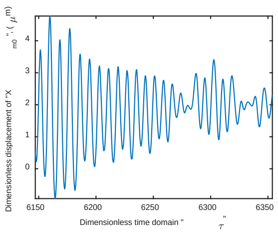

Time-domain response

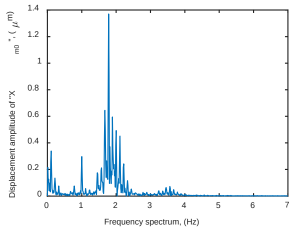

FFT spectrum

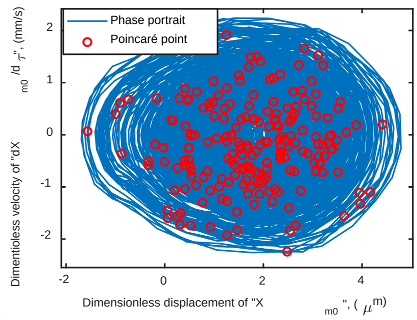

Phase plane and poincaré point

(b)The dynamic response of the system X_{m0} at 16000 rpm

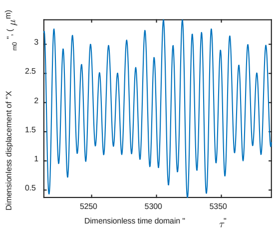

Time-domain response

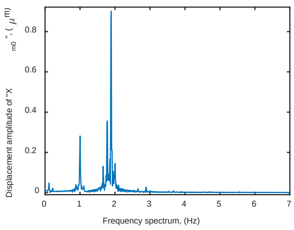

FFT spectrum

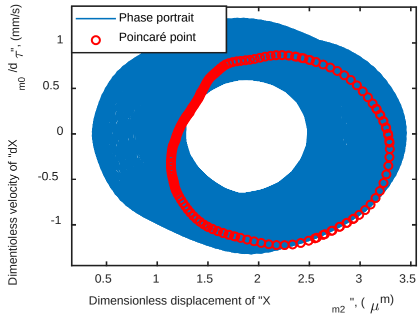

Phase plane and poincaré point

(c)The dynamic response of the system X_{m0} at 19800 rpm

Fig. 10. The dynamic response of the system X_{m0}

The effect of the rotating speed on the tow-speed gearbox at the (high) second-speed transmission condition

Considering the forward bifurcation map of the second condition that is shown in Figure 11 (a), it is detected that the system X_{m2} undergoes quasi-periodic motion at low speed within {1000-3250} rpm. The phase plane diagram is a disorder with a closed orbit formed by poincaré points (Gritli and Belghith, 2018), which is proved that the system X_{m2} behaves as quasi-periodic motion, as shown in Figure 12 (a). Then the system turns into chaotic motion through the quasi-periodic route at the speed range of {3291-3578} rpm. As illustrated in Figure 12 (b), the phase plane diagram shows irregular periodic motion. In general, the system X_{m2} keeps transforming between quasi-periodic and chaotic motions under the increasing of the rotational speed, where the system is in a state of chaos at the range speed of {4819-6156} rpm, {8065-8829} rpm, and {11030-11500} rpm. When the speed is about 11030 rpm and 11500 rpm in forwarding bifurcation, it is detected that the system X_{m2} contains both chaotic and quasi-period motion responses (Pan et al., 2019; Zhou et al., 2016; Gao et al., 2018). As proved in Figure 12 (c), at the rotating speed of 11025 rpm, the phase planes exhibit a relatively thick periodic motion, and the poincaré section shoes two clustered point set. Hence, the system X_{m2} is in the state of 1/2 subharmonic resonance (Wang, 2018). The system goes into chaotic regions through the quasi-periodic route around the range of {11030-11500} rpm. As illustrated in Figure 12 (d), the phase plane shows a highly disordered shape with discrete points created in the poincaré section. These vibration features demonstrate that the system X_{m2} exhibit chaotic motion.

(a)

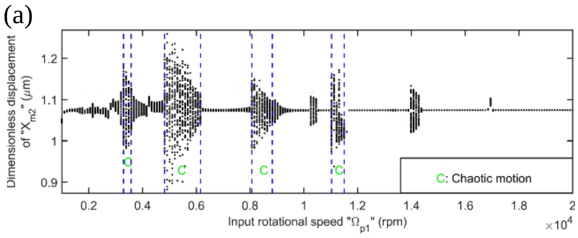

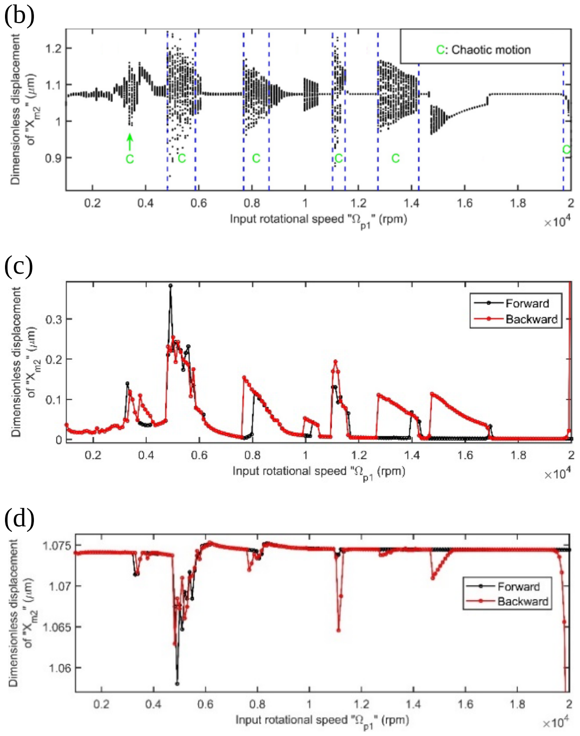

Fig. 11. The vibration diagrams of the system X_{m2} of the second-speed transmission using Ω_{p1} as a controller parameter: (a) forward bifurcation map, (b) backward bifurcation map, (c) PPV, (d) RMS

The system X_{m2} turns into quasi-periodic motion again and persists at the speed range of {11600-20000} rpm. As seen in Figure 12 (e), the phase plane diagram shows regular unrepeated curves motion causing the poincaré points to form a virtual circle shape Hopf circles (Zhang et al., 2008). Where the motions of the Hopf bifurcation points are quasi-periodic routes (Xiang et al., 2016). However, the pinion's rotating speed affects the responses of X_{m2}. The responses at the speed of 17000 rpm show a shifted phase portrait forming a two curve of poincaré point sets, which indicates that the response of X_{m2} is quasi-periodic motion (Zhao and Ji, 2015), as shown in Figure 12 (f).

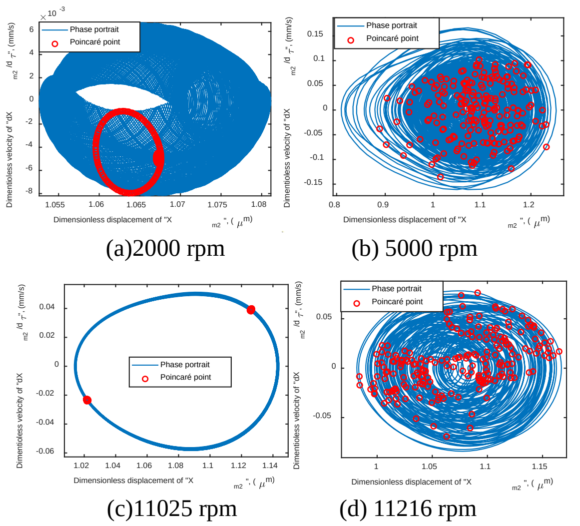

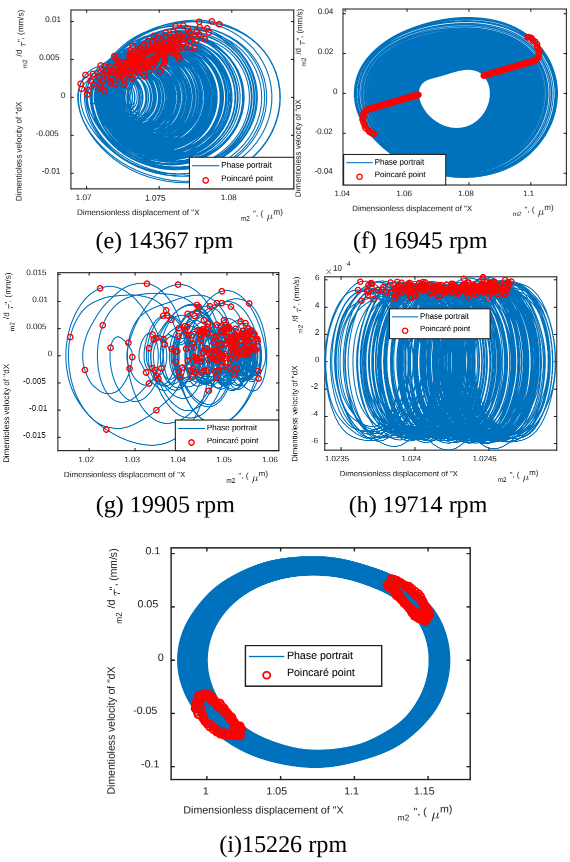

Fig. 12. The Phase plane and poincaré point of the system X_{m2}

It is observed that the response characteristics of the forward and backward bifurcation map of the system X_{m2} are identical. Considering the backward bifurcation map shown in Figure 11 (b), the chaotic motion range gets wider, especially at the corresponding speed range of {7683-8638} rpm, while new chaotic regions were detected at {12740-14270} rpm and {19710-20000} rpm. The chaotic motion range is diminished at a low speed of 3387 rpm. A ‘frequency hopping’ occurs at the speed of 14750 rpm during the backward sweep. These variations are also proven by apparent bistable found in the PPV map in Figure 11 (c) and (d).

During the backward sweep, the highest rotating speed within {19720-20000} rpm impacts fiercer at system X_{m2}. At a high-speed range within {19720-20000} rpm, the system starts at a highly disordered vibration response in the phase plane plot with non-periodic motion, translating the chaotic response, as shown in Figure 12 (g).

Both phase plane and poincaré section have shifted and unrepeated responses at 19714 rpm (Zhao and Ji, 2015), as demonstrated by Figure 12 (h). Thus, the system X_{m2} enters a chaotic region {19720-20000} rpm through quasi-periodic motion. With the decreasing of the pinion’s rotating speed, two attracting invariant curves emerge associated with quasi-periodic dynamics in the poincaré section as the rotating speed decrease within {14750-15320} rpm, hence the system X_{m2} performs a quasi-periodic solution (Liu et al., 2017), as displayed in Figure 12 (i).

The PPV and RMS responses curves of the system X_{m2} at the second condition are illustrated in Figure 11 (c) and (d), where the controller parameter is the pinion rotational speed. With the increase of rotational speed from 1000 rpm to 20,000 rpm (as forwarding sweep frequency), the amplitude value contains many jumps-up phenomena at {3291, 4819, 8065, 11030} rpm then turns into chaotic motions. The system also contains many jumps-down phenomena at {10260, 13980} rpm then turns into quasi-periodic motions. Moreover, hysteresis loops are observed clearly in PPV map; it is noted that there are three apparent bistable response regions at {7683-8065} rpm, {9975-10260} rpm, {12740-13980} rpm and {14750-16850} rpm. Considering the backward sweep frequency, the rotational speed of the pinion decreases from 20,000 rpm to 1000 rpm. The system keeps in a quasi-periodic state at high speed. With the decreasing of rotational speed, jumps up phenomena detected at {14180 and 55774} rpm then turns into chaotic motions, whereas jump up at 10450 rpm and goes into chaotic and periodic-2 motion; the system also contains many jumps down phenomena at {19900, 14750, 12740, 11030, 9975, 7683, 4819} rpm then turns into quasi-periodic motions.

(a)

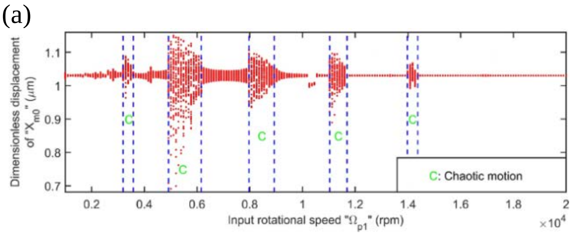

(b)

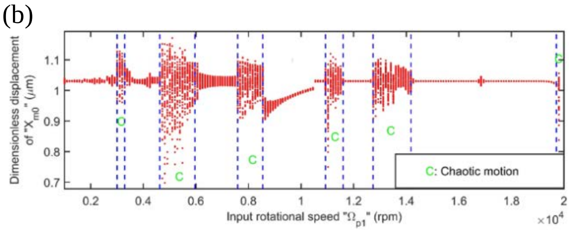

(c)

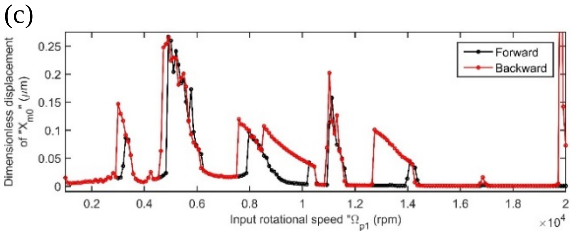

(d)

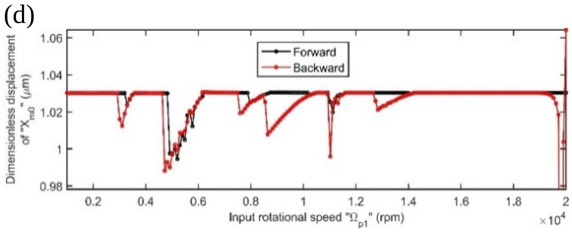

Fig. 13. The vibration diagrams of the system X_{m0} of the second-speed transmission using Ω_{p1} as a controller parameter: (a) forward bifurcation map, (b) backward bifurcation map, (c) PPV, (d) RMS.

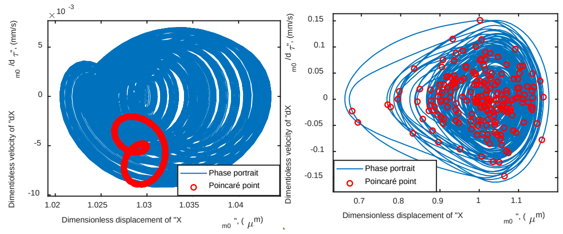

(a)2000 rpm (b) 5000 rpm

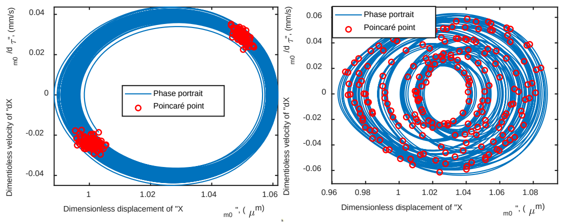

(c)10260 rpm (d) 13603 rpm

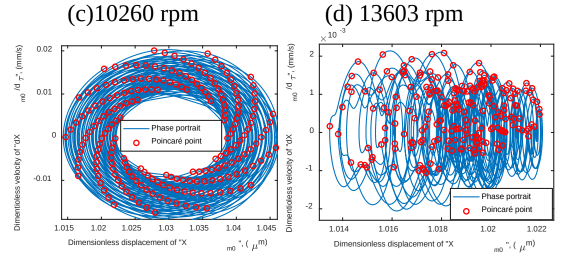

(e) 16850 rpm (f) 19709 rpm

Fig. 14. The Phase plane and poincaré point of the system X_{m0}

Figure 13 illustrates the forward and backward bifurcation, PPV, and RMS diagrams of the system X_{m0} at the second shifting condition. Considering the forward bifurcation map shown in Figure 13 (a), it is observed that the system response characteristics range is identical to the backward bifurcation map in Figure 13 (b). The chaotic motion range gets narrow, especially at the corresponding speed range of {3101-3387} rpm, {11030-11600} rpm, while its range gets wider at {11600-14180} rpm. Moreover, forward bifurcation has no chaotic motion at a high-speed range of {19710-20000} rpm compared with the chaotic response that exists in the backward bifurcation map, which is also proven by apparent bistable found in the PPV map in Figure 13 (c) and (d).

It is evident that the system X_{m0} is in quasi-periodic motion at low speed, where the system behaves as a quasi-periodic motion at a speed range of {1000-3100} rpm, {3578-4915} rpm, {6156-7870} rpm, and {8925-11030} rpm, as shown by the bifurcation diagrams in Figure 13 (a) and (b). As displayed in Figure 14 (a), the phase plane diagram has some closed-twisted and thick curves, the poincaré map also shows closed virtual curves. These results demonstrate that the system X_{m0} is in a quasi-periodic response. A short jump up and down phenomenon appears at 10260 rpm and 10550 rpm, respectively.

With the increase of the rotation speed, the system X_{m0} abandons the quasi-periodic motion comes into chaotic motion, and remains in chaos state at the range of {3196-3578} rpm, {4915-6156} rpm, {7970-8925} rpm, {11030-11690} rpm and {13980-14370} rpm. In this case, the phase planes are highly disordered with many discrete points shown in the poincaré section, as shown in Figure 14 (b). However, the system is in quasi-periodic-2 impact motion at the particular speed of 10260 rpm, as seen in Figure 14 (c). The phase plane exhibits a thick periodic motion, and the poincaré section shows two clustered points (Gritli and Belghith, 2018; Liu et al., 2017; Luo, 2004; Wen et al., 2008).

Considering the backward bifurcation, it is observed that the system X_{m0} is in a chaotic motion state within the speed range of {10930-11600} rpm and {12740-14180} rpm. Where the phase plane diagram is disordered with many discrete points shown in the poincaré section, as displayed in Figure 14 (d). However, when the speed is at the range of {14370-19620} rpm, the system undergoes quasi-periodic motions, where the poincaré maps form an unenclosed loop (Hu et al., 2018;C.W.Chang-Jian,2010) combined with several trajectories lined sets (Wang and Zhu, 2021) showed in the phase portrait, which proves the system X_{m0} has a quasi-periodic motion, as demonstrated in Figure 14 (e). All these characteristics indicate that the system X_{m0} enters the limit cycle motion (Hopf circles) (Zhang et al., 2008; Xu and Ji, 2019; Lv et al., 2021). Finally, the system X_{m0} ends with chaotic motion at a high-speed range of {19700-20000} rpm. The chaos state is detected due to the disordered shape in the phase plane, the scattered points shown in the poincaré section, as illustrated in Figure 14 (f).

The PPV and RMS responses of the system X_{m0} are shown in Figure 13 (c) and (d), where the controller parameter is the pinion rotational speed. With the increase of rotational speed from 1000 to 20,000 rpm (as forwarding sweep frequency), the amplitude value has many jumps up phenomena at {3291, 4915, 7970, 11030, 12840, 14080} rpm then turns into chaotic motions. Furthermore, hysteresis loops are observed clearly in PPV and RMS map. It is noted that there are three apparent bistable response regions in the system at {7588-7970}rpm, {8543-10260}rpm, {12740-14080} rpm and {19710-20000} rpm. Considering the backward sweep frequency, the rotational speed of the pinion decreases from 20,000 to 1000 rpm. The system X_{m0} is in a chaos state at high speed {19710-20000} rpm range then turns into quasi-periodic until 14180 rpm. With the decreasing of the rotational speed, jumps-up phenomena are detected at {11600, 14270} rpm then the system X_{m0} turns into chaotic motions. The system also contains many jumps-down phenomena at {12740, 11030, 8543, 7588, 4724, 3005} rpm then turns into quasi-periodic motions.

In summary, the dynamic response of the system X_{m2} and X_{m0} of the second condition are identical. Under the variation of the rotational speed, both system response fluctuates between the quasi-periodic and chaotic motion. Comparing the forward and backward bifurcation, the range of chaotic response of both systems X_{m2} and X_{m0} is smaller at the forward bifurcation and gets broader in the case of backward bifurcation, as proven by the apparent bistable response regions on PPV and RMS maps in Figure 13 (c) and (d).

The effects of system parameters on the tow-speed gearbox transmission

In this chapter, the effects of TVMS, bearing support stiffness, and STE amplitude on the response of the two-speed transmission system are analyzed to guide the optimization of the system's dynamic response.

To present the extent of variation in Formula (5), we execute the bifurcation diagram of the relative displacement of the first and second stage gear pair at the second condition under the variety of TVMS ratio k_o/A_k within (3.33-20), as shown in Figure 15 (a) and (b). The motion of the system X_{m2} and X_{m0} is chaotic when the mesh stiffness ratio k_o/A_k is small within (3.33-13.72). On the contrary, when the amplitude of the mesh stiffness ratio k_o/A_k increases within (13.72-20), the dynamic response of both system X_{m2} and X_{m0} turns into quasi-periodic motion. In summary, we conclude that the TVMS is considered a significant factor in the dynamic behavior of the TST gearboxes. Strong non-linear characteristics of the system's motion were revealed when the amplitude of the TVMS ratio k_o/A_k is small within (3.33-13.72) that is due to the low hardness of the gear surface; whereas the quasi-stable motion is easy to achieve when the TVMS ratio k_o/A_k is high within (13.72-20). According to this concept and in the actual engineering practice, high mesh stiffness can be reached via effective methods, such as strengthening surface hardness and appropriate tooth profile design.

Since supporting stiffness is a significant parameter that affects the system's dynamic response, it is essential to study the influence of support stiffness on TST's dynamic characteristics. The pinion's rotating speed Ω_{pi} and stiffness of bearing k_{ijv} are assigned as control parameters. $i = (x,y,z)$ are the axis directions. $j = (p,g)$ represent the pinion and gear. i = (1,2,0) donate the first, second, and (final) fixed gear-pair, respectively. Figure 16 shows the maximum Lyapunov exponents diagrams of the vibration displacement X_{m2} and X_{m0} when the supporting stiffness k_{ijv} is set to vary from low to high values 1×10^6 N/m, 3.5×10^7 N/m, and 8×10^9 N/m, respectively.

The maximum Lyapunov exponents depict that at low stiffness of 1×10^6 N/m the dynamic response has a more significant influence on the dynamic behaviors of both systems X_{m2} and X_{m0}. That is proven by the highest Lyapunov value corresponding to the speed range within {3101-3482} rpm, {7874-8447} rpm, and {10640-11310} rpm as for the system X_{m2}, as shown in Figure 16 (a); excluding the speed range of {3101-3482} rpm as for X_{m0} as shown in Figure 16 (b).

These high Lyapunov values indicate that the system response is chaotic and unstable, and the lower values close to the zero-line indicate the quasi-periodic motion. When the support stiffness increases to 3.5×10^7 N/m, the dynamic response of both systems corresponding to the previous rotating speed ranges has fewer effects compared with the dynamic response of lower stiffness of 1×10^6 N/m. However, the Lyapunov exponents of X_{m0} are greater corresponding to the speed range of {3101-3482}rpm and {5869-6347} rpm. When the support stiffness k_{ijv} = 8×10^9 N/m, the chaotic motions under the mentioned critical speed range disappear and turn into quasi-periodic motion. Meanwhile, new chaotic responses of both systems are revealed within the speed range of {6538-8065} rpm, as proven by the red curve shown in Figure 16. These dynamic response variations of both systems indicate that the support stiffness has a significant influence on the meshing state of the gear teeth. Hence, the bearing stiffness must be designed accordingly to eliminate the severe fluctuations of the system's dynamic response.

In short, the dynamic behavior of the gear system underwent an extensive range of chaotic motion at low bearing stiffness. However, the high amplitude (chaotic motion) of maximum Lyapunov exponents diminishes as the bearing stiffness increases, then entirely disappears and turns into quasi-periodic motion when further increasing bearing stiffness. This proves that the support stiffness could control the noise and vibration of the system in the practical engineering application. Hence, the obtained results reveal the significance of considering the non-linear effect of support gear when evaluating the dynamic response of a practical gearbox.

Figure 17 shows the maximum Lyapunov exponent plots under three different STE amplitudes. When the STE amplitude is equal to 20 µm, the chaotic motion regions are observed under the rotating speed of {3196-4724} rpm, {3578-6060} rpm, {7683-8543} rpm, and {10930-11600} rpm and proven by the high amplitude of the Lyapunov exponents. When the STE amplitude increases to 120 µm, the amplitude of the maximum Lyapunov exponents of both system X_{m2} and X_{m0} turns higher corresponding to the speed ranges of {3578-6060} rpm and {7683-8543} rpm, as displayed in Figure 4. The increases in the maximum Lyapunov exponents' amplitude indicate that the ranges of chaotic motion corresponding to these rotating speed ranges were enhanced. However, the chaotic region of the system X_{m2} corresponding to the speed ranges of {3578-6060} rpm {3578-6060} rpm enlarges, and the amplitude of Lyapunov exponent rases when the STE is increased to 300µm. Meanwhile, the range of chaotic motion of the system X_{m0} enlarges corresponding to the rotating speed of {4437-6251} rpm; the Lyapunov amplitude also rases under the speed of {3101-3482} rpm and {10930-11600} rpm, indicating that the range of chaotic motion was strongly enhanced.

In short, the TVMS ratio has more effect on the dynamic behavior of gearbox components compared to the other internal excitation source such as STE. When the STE amplitude is low (for instance E_j =20 µm), the response of both systems X_{m2} and X_{m0} seems relatively stable. When the STE amplitude is increased to 120 µm, the chaotic response of both systems becomes enhanced. When the STE amplitude is further increased to 300 µm, the chaotic motion response of both systems becomes more excited and enlarged, and the system's stability becomes worse. This conclusion is in agreement with the actual engineering practice. Hence, the gear's installation precision and manufacturing must be improved to achieve the system's stability.

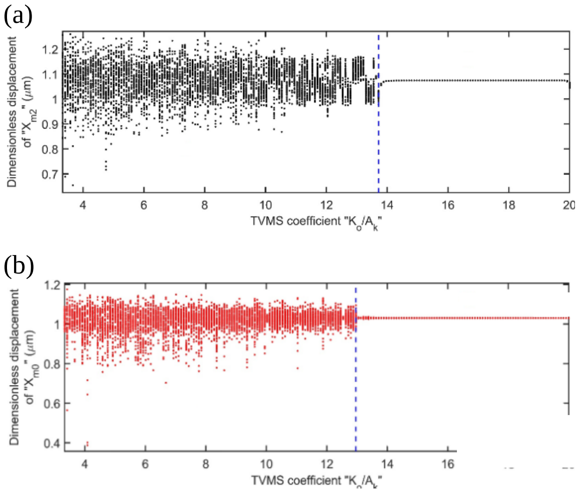

Fig. 15. The vibration diagrams using TVMS ratio k_o/A_k as control parameter when Ω_{pi} =11100 rpm: (a) X_{m2}, (b) X_{m0}.

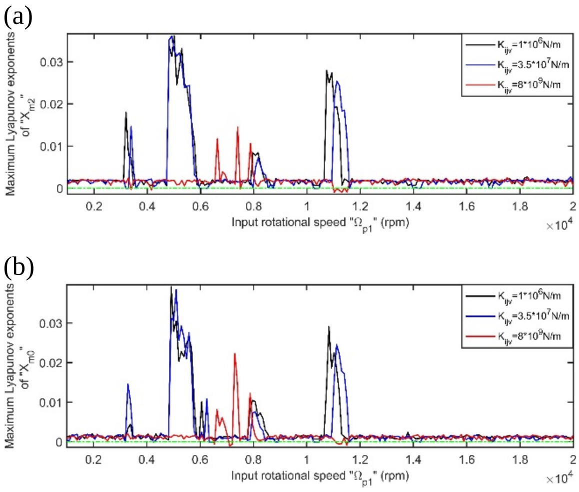

Fig. 16. The maximum Lyapunov exponents of system response using rotating speed Ω_{pi} and different support stiffness k_{ijv} as control parameters: (a) X_{m2}, (b) X_{m0}.

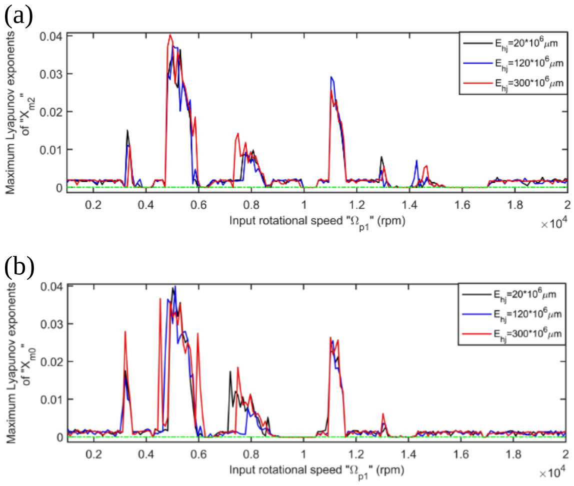

Fig. 17. The maximum Lyapunov exponents of system response using rotating speed Ω_{pi} and different STE E_j as control parameters: (a) X_{m2}, (b) X_{m0}.

CONCLUSIONS

In this paper, a multi-freedom non-linear dynamic model of a TSHG transmission equipped with a two-way synchronizer used in PEV was established. Which considers the TVMS, mesh damping, STE, transmission errors, gear backlash, and torsional damping and stiffness. An electric drive two-stage gear transmission test rig was established, and the effectiveness of the established dynamic model was verified through comparison. The non-linear dynamics of the gear system under two transmission condition was analyzed with the help of a global bifurcation map, maximum Lyapunov exponents, FFT spectra, poincaré map, time-domain history, phase portrait, RMS, and PPV. Where the effect of the pinion's rotating speed, TVMS ratio, and supporting stiffness on the system's dynamic responses was also analyzed. The obtained results provide a helpful reference and understanding of designing such systems. The following conclusions can be summarized as follows:

(1) From the study of the pinion's rotating speed and the dynamic response of the gear system at the second (high) speed transmission condition, it was found that the system exhibited complex non-linear dynamic characteristics compared with the first (low) speed transmission one. The results indicate the high speed over 14000 rpm affects the natural frequency of the gear pair system during the low-speed transmission condition. On the contrary, in the high-speed transmission condition, the system is hardly excited and reveals many chaotic regions corresponding to the pinion's rotating speed below 14000 rpm. It is found that the system enters into chaos via the quasi-periodic and double quasi-periodic routes. Where both systems exhibit various dynamic responses and phenomena such as quasi-periodic motion, double quasi-periodic motion, chaotic motion, Hopf bifurcation, frequency hopping, sub-harmonic, and hysteresis loop response.

(2) Based on the influence mechanism of TVMS on the dynamic response, it is noteworthy that the non-linear characteristics crisis on the system's motion were revealed when the amplitude of the TVMS ratio is small (3.33-13.72) due to the low hardness of the gear surface. The quasi-stable motion is easy to achieve when the TVMS ratio is higher about (13.72-20). According to this concept, in practical engineering practice, the mesh stiffness can be improved by effective methods to suppress vibration.

(3) According to the influence mechanism of bearing stiffness on the dynamic response, it was concluded that the changes in bearing stiffness have a significant influence on the meshing state of the gear teeth. The dynamic response underwent an extensive range of chaotic motion at low bearing stiffness. However, when the bearing stiffness increases, part of the chaotic motion decreases then disappears completely or even becomes quasi-periodic motion. Due to the significant influence of support stiffness on the gear system's meshing state, the bearing stiffness must be designed accordingly to eliminate the severe fluctuations of the system's dynamic response, hence, achieving the purpose of vibration control and extending the system life.

(4) Compared to the internal excitation source such as TVMS, the STE has less influence on the vibrations of gearbox components. It was found the increases of STE amplitude to 300 μm could enormously enhance and enlarges the chaos response of the gearbox system, leading the system's stability to become worse. Hence, the gear's installation precision and manufacturing must be improved to achieve the system's stability.

ACKNOWLEDGMENT

Conflicts of interest

The authors declare that they have no conflict of interest.

REFERENCES

Ahssan, M.R., Ektesabi, M. M., and Gorji, S.A., "Electric Vehicle with Multi-Speed Transmission: A Review on Performances and Complexities," *SAE International Journal of Alternative Powertrains*, Vol. 7, No. 2, pp. 169-182 (2018).

Aldo, S. et al., "A Novel Seamless 2-Speed Transmission System for Electric Vehicles: Principles and Simulation Results," *Sae International Journal of Engines*, vol. 4, no. 2, pp. 2671-2685 (2011).

Alizadeh, H.V. and Boulet, B., "Robust control of synchromesh friction in an electric vehicle's clutchless automated manual transmission," pp. 611-616 (2014).

Al Tayari, A.M.Y. and Chen, S. et al., "A Coupled Torsional-Transition Nonlinear Vibration and Dynamic Model of a Two-Stage Helical Gearbox Reducer for Electric Vehicles," *Shock and Vibration*, vol. 2020, p. 8838521, (2020).

Bartram, M., Mavros, G., and Biggs, S., "A study on the effect of road friction on driveline vibrations," *Proceedings of the Institution of Mechanical Engineers Part K Journal of Multi-body Dynamics*, vol. 1, no. K4, pp. 1-20 (2010).

Bozca, M., "Torsional vibration model based optimization of gearbox geometric design parameters to reduce rattle noise in an automotive transmission," *Mechanism and Machine Theory*, vol. 45, no. 11, pp. 1583-1598 (2010).

Bozca, M., "Transmission error model-based optimisation of the geometric design parameters of an automotive transmission gearbox to reduce gear-rattle noise," *Applied Acoustics*, vol. 130, pp. 247-259 (2018).

Bozca, M. and Fietkau, P., "Empirical model based optimization of gearbox geometric design parameters to reduce rattle noise in an automotive transmission," *Mechanism and Machine Theory* , vol. 45, no. 11, pp. 1599-1612 (2010).

Cao X., Du C., Yan F., Xu, H., He, B., and Sui, Y., "Parameter Optimization of Dual Clutch Transmission for an Axle-split Hybrid Electric Vehicle," *IFAC-PapersOnLine*, vol. 52, no. 5, pp. 423-430 (2019).

Chang Jian, C. W., "Strong nonlinearity analysis for gear-bearing system under non-linear suspension—bifurcation and chaos," *Nonlinear Analysis Real World Applications*, vol. 11, no. 3, pp. 1760-1774 (2010).

Chen, H., and Tian, G., "Modeling and analysis of engaging process of automated mechanical transmissions," *Multibody System Dynamics* , vol. 37, no. 4, pp. 345-369 (2016).

Chen, W., Chen, S., Hu, Z., Tang, J., and Li, H., "A novel dynamic model for the spiral bevel gear drive with elastic ring squeeze film dampers," *Nonlinear Dynamics,* vol. 98, no. 2, pp. 1081-1105 (2019).

Climent, H., Pla, B., Bares, P. and Pandey, V., " Exploiting driving history for optimising the Energy Management in plug-in Hybrid Electric Vehicles," *Energy Conversion and Management,* vol. 234, 113919 (2021).

Collins, J., Gourdin, G., and Qu, D., "Chapter 3.23 - Modern Applications of Green Chemistry: Renewable Energy," *in Green Chemistry, B. Török and T. Dransfield Eds*, pp. 771-860 (2018).

Desiree, Alcazar García., Jose, Luis. Romeral. Martínez, " Model-based design validation and optimization of drive systems in electric, hybrid, plug-in hybrid and fuel cell vehicles," *Energy*, vol. 254, p. 123719 (2022).

Di, N. F., Aldo, S., Thomas, H., Fabio, V., and Stefano, B., "Optimization of a Multiple-Speed Transmission for Downsizing the Motor of a Fully Electric Vehicle," *Sae International Journal of Alternative Powertrains*, vol. 1, no. 1, pp. 134-143 (2012).

Fan, B., Siyu, C., and Jinyuan, T., "Comparisons of dynamic responses of a spur gear pair with two forms of profile deviation," *Australian Journal of Mechanical Engineering*, vol. 18, no. 19, pp. 1-9 (2018).

Galvagno, E., Velardocchia, M., and Vigliani, A., "Analysis and simulation of a torque assist automated manual transmission," *Mechanical Systems and Signal Processing*, vol. 25, no. 6, pp. 1877-1886 (2011).

Gao, B., Liang, Q., Xiang, Y., Guo, L., and Chen, H., "Gear ratio optimization and shift control of 2-speed I-AMT in electric vehicle," *Mechanical Systems and Signal Processing*, vol. 50-51, pp. 615-631 (2015).

Gao, B., Meng, D., Shi, W., Cai, W., " Topology optimization and the evolution trends of two-speed transmission of EVs," *Renewable and Sustainable Energy Reviews*, vol. 161, p. 112390 (2022).

Gao, Xiang. Ling., Hu, Nan., and Aijun, "Dynamic analysis of a planetary gear system with multiple non-linear parameters," *Journal of Computational & Applied Mathematics* (2018).

Gritli, H., and Belghith, S., "Diversity in the non-linear dynamic behavior of a one-degree-of-freedom impact mechanical oscillator under OGY-based state-feedback control law: Order, chaos and exhibition of the border-collision bifurcation," *Mechanism & Machine Theory*, vol. 124, pp. 1-41 (2018).

Han, J.O., Shin, J.W., Kim, J.C., and Oh, S.H., "Design 2-Speed Transmission for Compact Electric Vehicle Using Dual Brake System," *Applied Sciences*, vol. 9, no. 9, p. 1793 (2019).

He, X., Zhou, X., Xue, Z., Hou, Y., Liu, Q., and Wang, R., "Effects of gear eccentricity on time-varying mesh stiffness and dynamic behavior of a two-stage gear system," *Journal of Mechanical Science and Technology*, vol. 33, no. 3, pp. 1019-1032, (2019).

Hong, J., Zhang, C., Chu, H., Gao, B., "Gear downshift control of inverse-automatic mechanical transmission of electric vehicle," *Green Energy and Intelligent Transportation*, vol. 1, p. 100005, (2022).

Hu, X., Hu, B., Zhang, F., Fu, B., Li, H., and Zhou, Y., "Influences of spline assembly methods on non-linear characteristics of spline–gear system," *Mechanism & Machine Theory,* vol. 127, pp. 33-51 (2018).

Huang, H., Teik, C., Lim, J., Wu, Ding, W., Pang, J., " Multitarget prediction and optimization of pure electric vehicle tire/road airborne noise sound quality based on a knowledge- and data-driven method," *Mechanical Systems and Signal Processing*, vol. 197, p. 110361, (2023).

İnci, M., Büyük, M., Demir, M.H., and İlbey, G., "A review and research on fuel cell electric vehicles: Topologies, power electronic converters, energy management methods, technical challenges, marketing and future aspects," *Renewable and Sustainable Energy Reviews*, vol. 137, p. 110648, (2021).

Jia, S., Howard, I., and Wang, J., "The Dynamic Modeling of Multiple Pairs of Spur Gears in Mesh, Including Friction and Geometrical Errors," *International Journal of Rotating Machinery,* vol. 9, no. 6, pp. 437-442 (2003).

Kahraman, A. and Singh, R., "Interactions between time-varying mesh stiffness and clearance non-linearities in a geared system," *Journal of Sound and Vibration,* vol. 146, no. 1, pp. 135-156 (1991).

Karunamoorthy, B., and Shobana, S., "Design and development of hybrid electric vehicle," Materials Today: Proceedings (2021).

Li, L., Wang, X., and Song, J., "Fuel consumption optimization for smart hybrid electric vehicle during a car-following process," *Mechanical Systems and Signal Processing*, pp. 1-10, (2016).

Li, L., Zhang, T., Sun, B., Wu, K., "Research on electro-hydraulic ratios for a novel mechanical-electro-hydraulic power coupling electric vehicle," *Energy*, vol. 270, p. 126970 (2023).

Liang, J., Yang, H., Wu, J., Nong, Z., and Walker, P.-D., "Shifting and power sharing control of a novel dual input clutchless transmission for electric vehicles," *Mechanical Systems and Signal Processing*, vol. 104, pp. 725-743 (2018).

Ling, J., Yang, H., Wu, J., Zhang, N., and Walker, P.-D., "Power-on shifting in dual input clutchless power-shifting transmission for electric vehicles," *Mechanism and Machine Theory*, vol. 121, pp. 487-501 (2018).

Liu, Y., Wang, Q., and Xu, H., "Analytical determination of bifurcations of periodic solution in three-degree-of-freedom vibro-impact systems with clearance," *Chaos Solitons & Fractals,* vol. 99, pp. 141-154 (2017).

Long, H., Wang, Z., Wang, J., Li, Y., "Research on the shift rule of two-speed transmission in pure electric van," *International Journal of Vehicle Systems Modelling and Testing,* vol. 16, p. 95-112 (2022).

Lovas, L., Play, D., Marialigeti, J., and Rigal, J.-F., "Mechanical Behaviour Simulation for Synchromesh Mechanism Improvements," *Proceedings of the Institution of Mechanical Engineers -- Part D*, vol. 220, no. 7, pp. 919-945 (2006).

Luo, G. W., "Period-doubling bifurcations and routes to chaos of the vibratory systems contacting stops," *Physics Letters A*, vol. 323, no. 3-4, pp. 210-217 (2004).

Lv, Z., Xu, H., and Bu, Z., "Control of Neimark Sacker bifurcation in a type of weak impulse excited centrifugal governor system," *International Journal of Non-Linear Mechanics* (2021).

Ma, B., Lu, W., Wang, H., and Yu, L., "Gearshift characteristics of a two-speed transmission using new electrically controlled toothed band brakes," *Journal of Mechanical Science and Technology* , vol. 36, p. 5821-5830 (2020).

Ma, J., Li, C., Liu, J., Cao,D., and Huang, J., "Experimental study on transmission error of space-driven gear system under large inertia load," *Advances in Mechanical Engineering* , vol. 11, no. 6, p. 168781401985695 (2019).

Ma. J., Li. C., and Cu. L., "Transmission Error Analysis and Disturbance Optimization of Two-Stage Spur Gear Space Driven Mechanism with Large Inertia Load," *Shock and Vibration* , vol. 2018, no. PT.6, pp. 1-14 (2018).

Mo, W., Walker, P.D., and Zhang, N., "Dynamic analysis and control for an electric vehicle with harpoon-shift synchronizer," *Mechanism and Machine Theory,* vol. 133, pp. 750-766 (2019).

Mo, W., Walker, P.D., Fang, Y., Wu, J., and Nong, Z., "A novel shift control concept for multi-speed electric vehicles," *Mechanical Systems and Signal Processing,* vol. 112 (2018).

Pan, W., Li, X., Wang, L., and Yang, Z., "Non-linear response analysis of gear-shaft-bearing system considering tooth contact temperature and random excitations," *Applied Mathematical Modelling* , vol. 68, no. APR., pp. 113-136 (2019).

Qiong et al., "The Seamless Gear Shifting Control for Pure Electric Vehicle with 2-speed Inverse-AMT," Ifac Proceedings Volumes (2013).

Raghothama, A.and Narayanan, S., "BIFURCATION AND CHAOS IN GEARED ROTOR BEARING SYSTEM BY INCREMENTAL HARMONIC BALANCE METHOD," *Journal of Sound and Vibration,* vol. 226, no. 3, pp. 469-492, (1999).

Rahimi Mousavi, M.S., Pakniyat, A., Wang, T., and Boulet, B., "Seamless dual brake transmission for electric vehicles: Design, control and experiment," *Mechanism and Machine Theory*, vol. 94, pp. 96-118 (2015).

Ruan, J., Walker, P., and Zhang, N., "A comparative study energy consumption and costs of battery electric vehicle transmissions," *Applied Energy*, vol. 165, pp. 119-134, (2016).

Tian, Y., Zhang, N., Zhou, S., and Walker, P.-D., "Model and gear shifting control of a novel two-speed transmission for battery electric vehicles," *Mechanism and Machine Theory*, vol. 152, p. 103902 (2020).

Tseng, C. Y., and Yu, C.H., "Advanced shifting control of synchronizer mechanisms for clutchless automatic manual transmission in an electric vehicle," *Mechanism & Machine Theory*, Vol.84, pp.37-56 (2015).

Wadallah, A et al, "Dynamic modelling and simulation of a manual transmission based mild hybrid vehicle," *Mechanism and Machine Theory: Dynamics of Machine Systems Gears and Power Trandmissions Robots and Manipulator Systems Computer-Aided Design Methods* (2017).

Walha, L., Driss, Y., Khabou, M.-T., Fakhfakh, T., and Hadda, M., "Effects of eccentricity defect on the non-linear dynamic behavior of the mechanism clutch-helical two stage gear," *Mechanism and Machine Theory*, vol. 46, no. 7, pp. 986-997 (2011).

Walha, L., Fakhfakh, T., and Haddar, M., "Non-linear dynamics of a two-stage gear system with mesh stiffness fluctuation, bearing flexibility and backlash," *Mechanism & Machine Theory*, vol. 44, no. 5, pp. 1058-1069 (2009).

Walker, P.D. and Nong, Z., "Engagement and control of synchroniser mechanisms in dual clutch transmissions," *Mechanical Systems & Signal Processing* , vol. 26, no. none, pp. 320-332 (2012).

Walker, P.-D. and Zhang, N., "Parameter study of synchroniser mechanisms applied to Dual Clutch Transmissions," *International Journal of Powertrain*s, vol. 1, no. 2, pp. 198-220 (2011).

Walker, P.D, Fang, Y., and Zhang, N., "Dynamics and control of clutchless automated manual transmissions for electric vehicles," Journal of Vibration & Acoustics (2017).

Wang, R.C. Hu, Wang, Z. Yan, F. and Chen, N., "Integrated optimal dynamics control of 4WD4WS electric ground vehicle with tire-road frictional coefficient estimation," Mechanical Systems and Signal Processing (2015).

Wang, X., " Stability research of multistage gear transmission system with crack fault," *Journal of Sound and Vibration*, vol. 434, no. 10, pp. 63-77 (2018).

Wang, J., Zhang, J., Yao, Z., Yang, X., Sun, R., and Zhao, Y., "Non-linear characteristics of a multi-degree-of-freedom spur gear system with bending-torsional coupling vibration," *Mechanical Systems and Signal Processing*, vol. 121, pp. 810-827 (2019).

Wang, S., and Zhu, R., "Non-linear dynamic analysis of GTF gearbox under friction excitation with vibration characteristics recognition and control in frequency domain," *Mechanical Systems and Signal Processin*g, vol. 151, p. 107373 (2021).

Wang, Y., Lü E., Lu, H., Zhang, N., and Zhou, X., "Comprehensive design and optimization of an electric vehicle powertrain equipped with a two-speed dual-clutch transmission," *Advances in Mechanical Engineering*, vol. 9, no. 1, p. 168781401668314 (2017).

Wang,Y., Zhang, S., Meng, D., Zhang, L., "Nonlinear overall annoyance level modeling and interior sound quality prediction for pure electric vehicle with extreme gradient boosting algorithm," *Applied Acoustics* , vol. 195, p. 108857, (2022).

Wen, G., Chen, S., and Jin, Q., "A new criterion of period-doubling bifurcation in maps and its application to an inertial impact shaker," *Journal of Sound & Vibration*, vol. 311, no. 1-2, pp. 212-223, (2008).

Xiang, L., Jia, Y., and Hu, A., "Bifurcation and chaos analysis for multi-freedom gear-bearing system with time-varying stiffness," *Applied Mathematical Modelling*, vol. 40, no. 23, pp. 10506-10520 (2016).

Xu, H., and Ji, J., "Analytical-numerical studies on the stability and bifurcations of periodic motion in the vibro-impact systems with clearances," *International journal of non-linear mechanics*, vol. 109, no. MAR., pp. 155-165 (2019).

Zhang, J. G., Yu, J.N., Chu, Y.D., Li, X.F. and Chang, Y.-X., " Bifurcation and chaos of a non-autonomous rotational machine systems," *Simulation Modelling Practice and Theory*, vol. 16, no. 10, pp. 1588-1605 (2008).

Zhang, H., Chen, D., Zhang, H., Liu, Y., "Research on the influence factors of brake regenerative energy of pure electric vehicles based on the CLTC," *Energy Reports* , vol. 8, p. 85-93, (2022).

Zhao, M. and Ji, J.C., "Non-linear torsional vibrations of a wind turbine gearbox," *Applied Mathematical Modelling* , vol. 39, no. 16, pp. 4928-4950, (2015).

Zhou, S., Song, G., Sun, M., and Ren, Z., "Non-linear dynamic response analysis on gear-rotor-bearing transmission system," *Journal of Vibration & Control* , vol. 24, no. 9, (2016).

APPENDIX A

The mass matrix $\left[\boldsymbol{M}\right]$ can be expressed by

$$[M]=\begin{bmatrix}
1&0&0&0&0&0&0&0&0&0&0&0&0&0&0&0&0&0\\
0&1&0&0&0&0&0&0&0&0&0&0&0&0&0&0&0&0\\
0&0&1&0&0&0&0&0&0&0&0&0&0&0&0&0&0&0\\
0&0&0&1&0&0&0&0&0&0&0&0&0&0&0&0&0&0\\
0&0&0&0&1&0&0&0&0&0&0&0&0&0&0&0&0&0\\
0&0&0&0&0&1&0&0&0&0&0&0&0&0&0&0&0&0\\
0&0&0&0&0&0&1&0&0&0&0&0&0&0&0&0&0&0\\
0&0&0&0&0&0&0&1&0&0&0&0&0&0&0&0&0&0\\
0&0&0&0&0&0&0&0&1&0&0&0&0&0&0&0&0&0\\
0&0&0&0&0&0&0&0&0&1&0&0&0&0&0&0&0&0\\
0&0&0&0&0&0&0&0&0&0&1&0&0&0&0&0&0&0\\
0&0&0&0&0&0&0&0&0&0&0&1&0&0&0&0&0&0\\
0&0&0&0&0&0&0&0&0&0&0&0&1&0&0&0&0&0\\
0&0&0&0&0&0&0&0&0&0&0&0&0&1&0&0&0&0\\
0&0&0&0&0&0&0&0&0&0&0&0&0&0&1&0&0&0\\
0&0&0&0&0&0&0&0&0&0&0&0&0&0&0&1&0&0\\
m_1&m_2&m_3&m_4&m_5&m_6&0&0&0&0&0&0&0&0&0&0&1&0\\
0&0&0&0&0&0&m_7&m_8&m_9&m_{10}&m_{11}&m_{12}&0&0&0&0&0&1
\end{bmatrix} \tag{A.1}$$

Here,

$$m_1=-a_{xi}, m_2=a_{yi}, m_3=a_{zi}, m_4=a_{xi}, m_5=-a_{yi}, m_6=-a_{zi}, m_7=-a_{x0}, m_8=a_{y0},$$
$$m_9=-a_{z0}, m_{10}a_{x0}, m_{11}=-a_{y0}, m_{12}=a_{z0} \tag{A.2}$$

For the sake of simplicity, the damping matrix $[\boldsymbol{C}]$ and the stiffness matrix $[\boldsymbol{K}]$ are expressed by $[\boldsymbol{\Lambda_{CK}}]$ as the following

$$[\Lambda_{CK}]=\begin{bmatrix}
\Lambda_1&0&0&0&0&0&0&0&0&0&0&0&0&0&0&0&\Lambda_2&0\\
0&\Lambda_3&0&0&0&0&0&0&0&0&0&0&0&0&0&0&\Lambda_4&0\\
0&0&\Lambda_5&0&0&0&0&0&0&0&0&0&0&0&0&0&\Lambda_6&0\\
0&0&0&\Lambda_6&0&0&0&0&0&0&0&0&0&0&0&0&\Lambda_8&0\\
0&0&0&0&\Lambda_9&0&0&0&0&0&0&0&0&0&0&0&\Lambda_{10}&0\\
0&0&0&0&0&\Lambda_{11}&0&0&0&0&0&0&0&0&0&0&\Lambda_{12}&0\\
0&0&0&0&0&0&\Lambda_{13}&0&0&0&0&0&0&0&0&0&0&\Lambda_{14}\\
0&0&0&0&0&0&0&\Lambda_{15}&0&0&0&0&0&0&0&0&0&\Lambda_{16}\\
0&0&0&0&0&0&0&0&\Lambda_{17}&0&0&0&0&0&0&0&0&\Lambda_{18}\\
0&0&0&0&0&0&0&0&0&\Lambda_{19}&0&0&0&0&0&0&0&\Lambda_{20}\\
0&0&0&0&0&0&0&0&0&0&\Lambda_{21}&0&0&0&0&0&0&\Lambda_{22}\\
0&0&0&0&0&0&0&0&0&0&0&\Lambda_{23}&0&0&0&0&0&\Lambda_{24}\\
0&0&0&0&0&0&0&0&0&0&0&0&\Lambda_{25}&0&0&0&\Lambda_{26}&0\\
0&0&0&0&0&0&0&0&0&0&0&0&0&\Lambda_{27}&0&0&\Lambda_{28}&\Lambda_{29}\\
0&0&0&0&0&0&0&0&0&0&0&0&0&0&\Lambda_{30}&\Lambda_{31}&0&\Lambda_{32}\\
0&0&0&0&0&0&0&0&0&0&0&0&0&0&\Lambda_{33}&\Lambda_{34}&0&0\\
0&0&0&0&0&0&0&0&0&0&0&0&\Lambda_{35}&\Lambda_{36}&0&0&\Lambda_{37}&0\\
0&0&0&0&0&0&0&0&0&0&0&0&0&\Lambda_{38}&\Lambda_{39}&0&0&\Lambda_{40}
\end{bmatrix} \tag{A.3}$$

where $\left[\boldsymbol{\Lambda}_{\mathbf{I}}\right]$ represents the damping and stiffness of the block $i=1,2,\cdots,40$, which can be expressed by the following equations

$$k_1=\frac{-k_{xpi}}{m_{pi}\omega_{ni}^2}, k_2=\frac{a_{xi}K_{mi}(\tau)}{m_{pi}\omega_{ni}^2}, k_3=\frac{-k_{ypi}}{m_{pi}\omega_{ni}^2},$$
$$k_4=\frac{-a_{yi}K_{mi}(\tau)}{m_{pi}\omega_{ni}^2}, k_5=\frac{-k_{zpi}}{m_{pi}\omega_{ni}^2}, k_6=\frac{-a_{zi}K_{mi}(\tau)}{m_{pi}\omega_{ni}^2},$$
$$k_7=\frac{-k_{xpi}}{m_{gi}\omega_{ni}^2}, k_8=\frac{-a_{xi}K_{mi}(\tau)}{m_{gi}\omega_{ni}^2}, k_9=\frac{-k_{ypi}}{m_{gi}\omega_{ni}^2},$$
$$k_{10}=\frac{a_{yi}K_{mi}(\tau)}{m_{gi}\omega_{ni}^2}, k_{11}=\frac{-k_{zpi}}{m_{gi}\omega_{ni}^2}, k_{12}=\frac{a_{zi}K_{mi}(\tau)}{m_{gi}\omega_{ni}^2},$$
$$k_{13}=\frac{-k_{xp0}}{m_{p0}\omega_{n0}^2}, k_{14}=\frac{a_{x0}K_{m0}(\tau)}{m_{p0}\omega_{n0}^2}, k_{15}=\frac{-k_{yp0}}{m_{p0}\omega_{n0}^2},$$
$$k_{16}=\frac{-a_{y0}K_{m0}(\tau)}{m_{p0}\omega_{n0}^2}, k_{17}=\frac{-k_{zp0}}{m_{p0}\omega_{n0}^2},$$
$$k_{18}=\frac{a_{z0}K_{m0}(\tau)}{m_{p0}\omega_{n0}^2}, k_{19}=\frac{-k_{xp0}}{m_{g0}\omega_{g0}^2},$$
$$k_{20}=\frac{-a_{x0}K_{m0}(\tau)}{m_{g0}\omega_{g0}^2}, k_{21}=\frac{-k_{yp0}}{m_{g0}\omega_{g0}^2},$$
$$k_{22}=\frac{a_{y0}K_{m0}(\tau)}{m_{g0}\omega_{g0}^2}, k_{23}=\frac{-k_{zp0}}{m_{g0}\omega_{g0}^2},$$
$$k_{24}=\frac{-a_{z0}K_{m0}(\tau)}{m_{g0}\omega_{g0}^2},$$
$$k_{25}=-\left(\frac{(K_0+K_s)A_m}{I_m\omega_{ni}^2}+\frac{(K_0+K_s)A_{pi}}{(I_{pi}+I_s)\omega_{ni}^2}\right),$$
$$k_{26}=\frac{K_{mi}(\tau)r_{pi}^2\cos(\beta_i)}{(I_{pi}+I_s)\omega_{ni}^2},$$

$$k_{27}=-\left(\frac{-K_{11}B_{gi}}{I_{gi}\omega_{ni}^2}+\frac{K_{11}B_{p0}}{I_{p0}\omega_{n0}^2}\right),$$
$$k_{28}=\frac{-K_{mi}(\tau)r_{gi}^2\cos(\beta_i)}{I_{gi}\omega_{ni}^2},$$
$$k_{29}=\frac{-K_{m0}(\tau)r_{p0}^2\cos(-\beta_0)}{I_{p0}\omega_{n0}^2},$$
$$k_{30}=-\left(\frac{-K_2B_{g0}}{I_{g0}\omega_{n0}^2}+\frac{K_2E_h}{I_h\omega_{n0}^2}\right),$$
$$k_{31}=\frac{K_3E_h}{I_h\omega_{n0}^2},k_{32}=\frac{K_{m0}(\tau)r_{g0}^2\cos(-\beta_0)}{I_{p0}\omega_{n0}^2},$$
$$k_{33}=\frac{K_2D_h}{I_h\omega_{n0}^2},k_{34}=-\left(\frac{K_3E_h}{I_h\omega_{n0}^2}+\frac{K_3E_v}{I_v\omega_{n0}^2}\right),$$
$$k_{35}=\frac{(K_0+K_s)A_{pi}\cos(\beta_i)}{(I_{pi}+I_s)\omega_{ni}^2},$$
$$k_{36}=\frac{-K_{11}B_{gi}\cos(\beta_i)}{I_{gi}\omega_{ni}^2},$$
$$k_{37}=-\left(\frac{r_{pi}^2}{(I_{pi}+I_s)}+\frac{r_{gi}^2}{I_{gi}}\right)\frac{K_{mi}(\tau)\cos^2(\beta_i)}{\omega_{ni}^2},$$
$$k_{38}=\frac{-K_{11}B_{p0}}{I_{p0}\omega_{n0}^2},k_{39}=\frac{K_2D_{g0}\cos(-\beta_0)}{I_{g0}\omega_{n0}^2},$$
$$k_{40}=-\left(\frac{r_{p0}^2}{I_{p0}\omega_{n0}^2}+\frac{r_{g0}^2}{I_{g0}}\right)\frac{K_{m0}(\tau)\cos^2(-\beta_0)}{\omega_{n0}^2}. \tag{A.4}$$

$$c_1=\frac{-c_{xpi}}{m_{pi}\omega_{ni}},c_2=\frac{a_{xi}c_{mi}}{m_{pi}\omega_{ni}},c_3=\frac{-c_{ypi}}{m_{pi}\omega_{ni}},$$
$$c_4=\frac{-a_{yi}c_{mi}}{m_{pi}\omega_{ni}},c_5=\frac{-c_{zpi}}{m_{pi}\omega_{ni}},c_6=\frac{-a_{zi}c_{mi}}{m_{pi}\omega_{ni}},$$
$$c_7=\frac{-c_{xpi}}{m_{gi}\omega_{ni}},c_8=\frac{-a_{xi}c_{mi}}{m_{gi}\omega_{ni}},c_9=\frac{-c_{ypi}}{m_{gi}\omega_{ni}},$$
$$c_{10}=\frac{a_{yi}c_{mi}}{m_{gi}\omega_{ni}},c_{11}=\frac{-c_{zpi}}{m_{gi}\omega_{ni}},c_{12}=\frac{a_{zi}c_{mi}}{m_{gi}\omega_{ni}},$$
$$c_{13}=\frac{-c_{xp0}}{m_{p0}\omega_{n0}},c_{14}=\frac{a_{x0}c_{m0}}{m_{p0}\omega_{n0}},c_{15}=\frac{-c_{yp0}}{m_{p0}\omega_{n0}},$$
$$c_{16}=\frac{a_{y0}c_{m0}}{m_{p0}\omega_{n0}},c_{17}=\frac{-c_{zp0}}{m_{p0}\omega_{n0}},c_{18}=\frac{-a_{z0}c_{m0}}{m_{p0}\omega_{n0}},$$
$$c_{19}=\frac{-c_{xp0}}{m_{g0}\omega_{n0}},c_{20}=\frac{-a_{y0}c_{m0}}{m_{g0}\omega_{n0}},c_{21}=\frac{-c_{yp0}}{m_{g0}\omega_{n0}},$$
$$c_{22}=\frac{a_{z0}c_{m0}}{m_{g0}\omega_{n0}},c_{23}=\frac{-c_{zp0}}{m_{g0}\omega_{n0}},$$
$$c_{24}=\frac{-c_{m0}\sin(-\beta_0)}{m_{g0}\omega_{n0}},$$
$$c_{25}=\left(\frac{(c_0+c_m)A_m}{I_m\omega_{ni}}+\frac{(c_0+c_m)A_{pi}}{(I_{pi}+I_s)\omega_{ni}}\right),$$
$$c_{26}=\frac{c_{mi}r_{pi}^2\cos(\beta_i)}{(I_{pi}+I_s)\omega_{ni}},$$
$$c_{27}=\left(\frac{c_{11}B_{gi}}{I_{gi}\omega_{ni}}+\frac{c_{11}B_{p0}}{I_{p0}\omega_{n0}}\right),c_{28}=\frac{-c_{mi}r_{gi}^2\cos(\beta_i)}{I_{gi}\omega_{ni}},$$
$$c_{29}=\frac{-c_{m0}r_{p0}^2\cos(-\beta_0)}{I_{p0}\omega_{n0}},$$
$$c_{30}=-\left(\frac{(c_2+c_t)D_{g0}}{I_{g0}\omega_{n0}}+\frac{(c_2+c_t)D_h}{I_h\omega_{n0}}\right),$$
$$c_{31}=\frac{c_3E_h}{I_h\omega_{n0}},c_{32}=\frac{c_{m0}r_{g0}^2\cos(-\beta_0)}{I_{g0}\omega_{n0}},$$
$$c_{33}=\frac{(c_2+c_t)D_h}{I_h\omega_{n0}},c_{34}=-\left(\frac{c_3E_h}{I_h\omega_{n0}}+\frac{c_3E_v}{I_v\omega_{n0}}\right),$$
$$c_{35}=\frac{(c_0+c_m)A_{pi}}{(I_{pi}+I_s)\omega_{ni}},c_{36}=\frac{-c_{11}B_{gi}}{I_{gi}\omega_{ni}},$$
$$c_{37}=-\left(\frac{r_{pi}^2}{(I_{pi}+I_s)}+\frac{r_{gi}^2}{I_{gi}}\right)\frac{c_{mi}\cos^2(\beta_i)}{\omega_{ni}},$$
$$c_{38}=\frac{-c_{11}B_{p0}}{I_{p0}\omega_{n0}},c_{39}=\frac{(c_2+c_t)D_{g0}}{I_{g0}\omega_{n0}},$$
$$c_{40}=-\left(\frac{r_{p0}^2}{I_{p0}}+\frac{r_{g0}^2}{I_{g0}}\right)\frac{c_{m0}\cos(-\beta_0)}{\omega_{n0}}. \tag{A.5}$$

The simplified coordinate vectors $\{Q_m\}$ and the vector force $\{F_Q\}$ can be written as

$$\{Q_m\}=\{X_{pi},Y_{pi},Z_{pi},X_{gi},Y_{gi},Z_{gi},X_{p0},Y_{p0},Z_{p0},X_{g0},Y_{g0},Z_{g0},X_a,X_b,X_d,X_e,X_{mi},X_{m0}\}^T \tag{A.6}$$

$$\{F_Q\}=\left[0,0,0,0,0,0,0,0,0,0,0,0,\left(\frac{r_m(T_m-T_{si})}{I_mS_i\omega_{ni}^2}-\frac{r_{pi}T_{si}}{(I_{pi}+I_s)S_i\omega_{ni}^2}\right),0,0,\frac{r_vT_{load}}{I_vS_0\omega_{n0}^2},,\left(\frac{r_{pi}T_{si}\cos(\beta_i)}{(I_{pi}+I_s)S_i\omega_{ni}^2}-\ddot{E}_i(\tau)\right),\ddot{E}_0(\tau)\right]^T \tag{A.7}$$

帶雙向同步器的雙速斜齒輪傳動非線性動力學模型及分析

童林軍[*] 王帝[**] 陳思雨[**] 孫周[**]

[*]佛山職業技術學院汽車工程學院

[**]中南大學機電學院

摘 要

爲了應對環境壓力和市場需求，多級變速器是純電動汽車可行的傳動方式。同步器可以有效降低頻繁換擋時純電動汽車的振動衝擊，但其缺乏理論模型限制了影響機理的進一步研究。爲此，考慮雙向同步器的剛度和摩擦力矩、時變齧合剛度、齧合阻尼、靜態傳動誤差、齒輪間隙、扭轉阻尼和剛度，建立了帶雙向同步器的雙速斜齒輪傳動的20自由度非線性動力學模型。與實驗結果的對比表明了所建立的動力學模型的有效性。動力學特性分析結果表明，與(低速)一擋相比，(高速)二擋表現出複雜的非線性動力學特性。支撐剛度的增加、時變齧合剛度比和靜態傳動誤差幅值的減小有助於系統混沌運動的減弱和消失。研究結果爲電動汽車雙速變速器的非線性行为抑制和減振降噪提供了有益的參考。